Corresponding Author: Dr. Jordi Roca-Sancho, Ph.D.

Corresponding Author's Institution: Universitat Politècnica de Catalunya

First Author: Jordi Roca-Sancho, Ph.D.

Order of Authors: Jordi Roca-Sancho, Ph.D.; Marc Berenguer, PhD; Daniel Sempere-Torres, PhD

Abstract: Dense radar networks offer the possibility of getting better Quantitative Precipitation Estimates (QPE) than those obtained with individual radars, as they allow increasing the coverage and improving quality of rainfall estimates in overlapping areas. Well-known sources of error such as attenuation by intense rainfall or errors associated with range can be mitigated through radar composites. Many compositing techniques are devoted to operational uses and do not exploit all the information that the network is providing. In this work an inverse method to obtain high-resolution radar reflectivity composites is presented. The method uses a model of radar sampling of the atmosphere that accounts for path attenuation and radar measurement geometry.
Two significantly different rainfall situations are used to show detailed results of the proposed inverse method in comparison to other existing methodologies. A quantitative evaluation is carried out in a 12h-event using two independent sources of information: a radar not involved in the composition process and a raingauge network. The proposed inverse method shows better performance in retrieving high reflectivity values and reproducing variability at convective scales than existing methods.

1

2

3

4

5

An inverse method to retrieve 3D radar reflectivity

composites

8

Jordi Roca-Sancho*, Marc Berenguer, Daniel Sempere-Torres

Centre de Recerca Aplicada en Hidrometeorologia, Universitat Politècnica de Catalunya, Barcelona (Spain).

11

12

13

14

15

16

17   *Corresponding author:

18   Jordi Roca-Sancho

19   E-mail address: jordi.roca(at)crahi.upc.edu

20   Phone number: +34616064983

21   Postal Address:

22   Centre de Recerca Aplicada en Hidrometeorologia-Universitat Politècnica de Catalunya.

23   Jordi Girona, 1-3, Edifici ParcUPC-K2M, S104

24   Barcelona E08034

25   Spain.

26   **Abstract**

27   Dense radar networks offer the possibility of getting better Quantitative Precipitation

28   Estimates (QPE) than those obtained with individual radars, as they allow increasing the

29   coverage and improving quality of rainfall estimates in overlapping areas. Well-known sources of

30   error such as attenuation by intense rainfall or errors associated with range can be mitigated

31   through radar composites. Many compositing techniques are devoted to operational uses and do

32   not exploit all the information that the network is providing. In this work an inverse method to

33   obtain high-resolution radar reflectivity composites is presented. The method uses a model of

34   radar sampling of the atmosphere that accounts for path attenuation and radar measurement

35   geometry.

36   Two significantly different rainfall situations are used to show detailed results of the

37   proposed inverse method in comparison to other existing methodologies. A quantitative

38   evaluation is carried out in a 12h-event using two independent sources of information: a radar

39   not involved in the composition process and a raingauge network. The proposed inverse method

40   shows better performance in retrieving high reflectivity values and reproducing variability at

41   convective scales than existing methods.

42

43   KEYWORDS: Weather radar; Radar network; Rain; Composite; Path attenuation;

44   Quantitative Precipitation Estimation

45

1. Introduction

Quantitative Precipitation Estimation (QPE) has been one of the main applications of weather radars since its early stages. Sources of error in radar rainfall estimation have been identified (e.g. Zawadzki, 1984) and many efforts have been devoted to analyze and mitigate them (see a review of the state of the art in Villarini and Krajewski, 2010). However, and in spite of the recent progress in radar data correction algorithms and better knowledge on the physics underlying the radar measurement process, there is still room for improvement.

Together with advancements in QPE schemes based on individual radars, the number of radars deployed around the world is increasing. This fact results in networks with larger coverage and areas where multiple observations are available. In these areas, sources of errors such as beam blockage, path attenuation by rain or errors associated with distance can be mitigated (Chandrasekar and Lim, 2008). Frequently, rainfall estimates from radar networks are obtained in composites built by picking the estimate from one of the radars at each grid point. This selection is done with criteria such as the maximum value (as an attempt to compensate for strong attenuation or beam blockage) or the observation from the closest radar (which considers the distance to the radar as the main error-driving factor). Other options presented in the literature are the criterion of minimum distance to the surface (Michelson et al., 2000) or the combination of the available observations based on quality indices (Fornasiero et al., 2006; Peura and Koistinen, 2007), which require a definition of a priori quality descriptors of each observation. Similarly, Zhang et al. (2005) proposed a distance-weighted mean for constructing three-dimensional reflectivity composites. Also, other recent advancements impose temporal continuity between the composites as an additional constraint (Langston et al., 2007; Peura, 2010).

In this work, we propose an alternative compositing technique accounting for the sources of error in radar observations. The method uses a model that simulates how a radar measures the precipitation field. Such a model is constructed for each radar of the network using the radar

3

71 equation (see e.g. Doviak and Zrnic, 1992). Following the concept of an inverse method (Menke,

72 1989), the proposed method retrieves the most realistic field given the observations of the radars

73 of the network. The simulation model used here accounts for the effects of beam broadening and

74 path attenuation by intense rain which is of particular interest in European networks, where

75 single polarization radars at attenuating wavelengths are numerous (e.g. Tabary et al., 2009).

76 Furthermore, we have evaluated the proposed inverse method for constructing high-

77 resolution 3D composites and compared it with the technique proposed by Zhang et al. (2005)

78 based on a distance-weighted mean. The high density of the radar network in the Barcelona area

79 is an appropriate environment for a systematic evaluation of the results using independent

80 information: provided that the region is covered with observations from three radars, we have

81 obtained a 3D reflectivity composite with the observations of two radars, and we have then

82 compared the results with the observations of the third radar, not involved in the composition.

83 On the other side, the analyzed compositing techniques have been evaluated in terms of rain

84 accumulations by comparison with raingauge measurements.

85 This paper is organized as follows: The region of interest and case studies are presented in

86 Section 2.1 together with the radar data used. Section 2.2 introduces two existing compositing

87 techniques used as reference. The proposed methodology is presented in Section 3. The

88 consistency of the inverse method is analyzed in Section 4. Section 5 includes a comparison of

89 the results against observations of an independent radar while in Section 6 a raingauge network is

90 used for evaluation. Section 7 summarizes the conclusions and includes further discussion.

91 ## 2. Setup of the experiment

92 *2.1. Data used*

93 The radar data used in this study were recorded with three C-band Doppler radars in the

94 vicinity of Barcelona, Spain. Hereafter, we will refer to them as LMI, CDV and BAR radars, and

95   their locations are, respectively, the summit of La Miranda, the Creu del Vent hill, and the Puig

96   d'Agulles hill near Barcelona (see Figure 1). LMI and CDV radars belong to the Meteorological

97   Service of Catalonia (SMC), and the BAR radar is part of the network of the Spanish Agency of

98   Meteorology (AEMET). The distance between LMI and CDV radars is 72 km, while the BAR

99   radar is, respectively, 90 and 45 km away from them. The main characteristics of these three

100 radars are summarized in Table 1.

101   The self-consistency of the developed methodology has been analyzed over two reflectivity

102 volume scans taken during two different events. The first case corresponds to a convective

103 situation that occurred during 17 and 18 September 2009, especially interesting for the presence

104 of convective cells in the area covered by the two radars (a large number of lightning discharges

105 were measured with the SMC sensors in the area on 17 September 2009 between 1800 UTC and

106 2100 UTC; SMC, 2009). The selected volume scans correspond to 2006 UTC September 2009.

107 The second case is a mainly stratiform event occurred between 4 and 6 February 2010; the

108 selected volume scans were recorded on 4 February 2010 at 1430 UTC.

109   The evaluation of the inverse method has been carried out with radar data that were

110 recorded on 2 November 2008 between 0000 and 1200 UTC. During this event, SMC reported

111 "abundant rainfall" (SMC, 2009) and the occurrence of damaging winds of convective origin [an

112 F2 tornado and a microburst was described by Bech et al. (2011)]. LMI and CDV radars have

113 been used to generate the composites, while BAR radar observations have served as an

114 independent source of information for the evaluation.

115   Ground clutter has been removed from all radar data using the techniques of Berenguer et

116 al. (2006) and Sánchez-Diezma (2001) and the effect of beam blockage has been reduced using

117 the technique of Delrieu et al. (1995). This guarantees the use of non-contaminated reflectivity

118 measurements (i.e. only associated with meteorological targets). Radar data have also been

119 adjusted by comparison with the records of a raingauge network to partially compensate for

120 radar calibration offsets (similarly as Delrieu et al., 2005). The comparison is done in terms of

121 total event rainfall accumulations –using the Marshall-Palmer Z-R relationship (Marshall and

122 Palmer, 1948). The comparison has been done near the radars and avoiding the areas most

123 affected by attenuation. Finally, further refinement has been performed by comparing reflectivity

124 distributions among the radars to avoid possible calibration differences.

125   Time differences among the PPIs of a volume scan have been partially compensated; the

126 motion field of each elevation has been estimated and the corresponding reflectivity field has

127 been shifted to a common time reference using the Lagrangian extrapolation technique of

128 Berenguer et al. (2011) in polar coordinates. This has also permitted to synchronize the

129 observations of the three radars at each time step.

130   Reflectivity retrievals are obtained in a 74.5 km x 74.5 km x 7 km domain and with a grid

131 spacing of 500 meters in the horizontal and 250 meters in the vertical. This resolution is a

132 compromise between the necessary representation of the atmosphere for the simulation model

133 and the computational cost. The area covered by this grid includes both LMI and CDV radar

134 locations (see Figure 1). For the evaluation using the independent BAR radar, the domain has

135 been extended 20 km to the East to include this radar.

136   *2.2. Existing 3D compositing schemes*

137   A number of radar composite techniques can be found in the literature, many of them

138 generating 2D mosaics. We compare the results of the proposed methodology with two 3D

139 compositing methods: (M1) the maximum value technique, widely used in operational systems,

140 and (M2) a distance-weighted mean of the multiple observations at a point, as proposed by

141 Zhang et al. (2005) after studying different possibilities for a 3D mosaic with the Weather

142 Surveillance Radar-1988 Doppler (WSR-88D) network.

143   2.2.1. M1: MAXIMUM VALUE TECHNIQUE

144   In a first step, observations of both LMI and CDV radars are converted from polar

145   coordinates to the 3D Cartesian grid introduced in Section 2.1. Such a conversion is done by

146   picking the nearest neighbor observation, which preserves extreme values and small-scale

147   variability (as discussed by Trapp and Doswell, 2000). Then, in each point of the grid, the two

148   reflectivity values corresponding to the converted observations of the two radars are compared;

149   and the maximum reflectivity value is assigned to the grid point. This process is illustrated in

150   Figure 2.

151   2.2.2. M2: DISTANCE-WEIGHTED MEAN

152   Zhang et al. (2005) proposed a 3D compositing scheme for the WSR-88D network with the

153   aim to fulfill the requirements of realistic representation of convective-scale features of rainfall at

154   a low computational cost. They studied four interpolation approaches to remap polar radar data

155   to Cartesian coordinates and found that for convective storms vertical interpolation provides the

156   most physically-realistic mosaic, while for widespread precipitation an additional horizontal

157   interpolation scheme was the best compromise. To compose measurements from several radars

158   at each grid point they finally chose a distance-weighted mean.

159 **3. Methodology**

160   The concept of using two or more radars to improve reflectivity estimates has been studied

161   in the past. Testud and Amayenc (1989) and Kabèche and Testud (1995) proposed a variational

162   method to estimate specific attenuation and reflectivity using two radars pointing to the same

163   precipitation volumes. Srivastava and Tian (1996) found an analytical solution to retrieve the

164   specific attenuation field using also two radars. Focused to the application in networked radar

165   environments (with two or more radars), Chandrasekar and Lim (2008) proposed a different

166   iterative method to retrieve reflectivity and specific attenuation for the X-band radar network of

7

167   CASA (Center for Collaborative Adaptive Sensing of the Atmosphere). On the other hand,

168   Andrieu and Creutin (1995) proposed an inverse method to obtain vertical profiles of reflectivity

169   accounting for the radar beam broadening and the power distribution within the beam for single

170   radar measurements.

171   Similarly, we propose here an inverse method to retrieve reflectivity composites using a

172   model of the radar sampling of the atmosphere and constrained to the observations from the

173   different radars of a network.

174   *3.1. Formulation of the inverse method*

175   The inverse method is based on the minimization of a cost function that penalizes

176   discrepancies between the actual observations at a given time and the simulations of the radar

177   sampling performed over the retrieved field for that time. We define the cost function for 2

178   radars (LMI and CDV) as:

$$J(z,\mathbf{a}) = \left\| dB[Z_{LMI}] - dB\left[\tilde{Z}_{m,LMI}(z,\mathbf{a})\right] \right\|^2 + \left\| dB[Z_{CDV}] - dB\left[\tilde{Z}_{m,CDV}(z,\mathbf{a})\right] \right\|^2 \qquad (1)$$

179   Where z is the retrieved high-resolution 3D reflectivity field, $\mathbf{a}$ are parameters determining

180   the relationship between specific attenuation (k) and non-attenuated reflectivity (z) as a function

181   of position (see the details in Section 3.3), Z_l is the volumetric reflectivity scan observed with the

182    $l = [LMI, CDV]$ radar, $\tilde{Z}_{m,l}(z,\mathbf{a})$ is the simulated volumetric reflectivity scan for the $l =$

183    $[LMI, CDV]$ radar, $dB[\cdot]$ is the operator $10\log(\cdot)$ and $\left\| dB[Z_l] - dB\left[\tilde{Z}_{m,l}(z,\mathbf{a})\right] \right\|$ stands for

184   the Euclidean distance between observed and simulated reflectivity volumes in logarithmic units

185   (dBZ). Hereafter, we will refer to z as the retrieved reflectivity field or the *composite* obtained with

186   the inverse method, and to $dB[Z_l]$, and $dB\left[\tilde{Z}_{m,l}(z,\mathrm{a})\right]$ as, respectively, the *observation* and the

187   *simulation* over the z field of the corresponding radar $l = [LMI, CDV]$.

8

3.2. Simulation of the radar sampling of the atmosphere

189   Simulations are carried out using a model that reproduces the radar sampling of the

190   atmosphere considering the characteristics of each radar (location, beam width, pulse length,

191   scanning strategy, etc.), power distribution within the radar beam, and path attenuation by

192   precipitation. Similar simulations were used by Sánchez-Diezma (2001), Bellon et al. (2005) or

193   Berenguer and Zawadzki (2008; 2009) to analyze the errors associated with range.

194   Given a 3D reflectivity field, a complete volume scan is simulated with the model for each

195   radar. The simulation model is based on the radar equation and the propagation of the radar

196   beams is assumed to follow the 4/3-effective Earth radius model (Doviak and Zrnic, 1992). For a

197   given elevation and azimuth, Equation 2 expresses the reflectivity simulated at range r, $\tilde{Z}_m(z,r)$,

198   as a function of the high-resolution 3D reflectivity field z:

$$\tilde{Z}_m(z,r) = \tilde{Z}(z,r) \cdot e^{\left[-0.46\int_0^r \tilde{K}(z,\mathbf{a},r)ds\right]}$$

$$\tilde{Z}(z,r) = \frac{\int_{V(r)}|W|^2 f^4 z \, dV}{\int_{V(r)}|W|^2 f^4 \, dV} \tag{2}$$

199   Where $\tilde{Z}(z,r)$ is the intrinsic (unattenuated) reflectivity in mm^{6}m^{-3} at range r (smoothed

200   according to the power distribution within the beam), $\tilde{K}(z,\mathbf{a},r)$ is the specific attenuation in

201   dB/km at range r (including the effect of the power distribution within the beam; see Section 3.3

202   for the description of the attenuation model), $V(r)$ is the radar sampling volume at range r, $|W|^2$

203   and f^4 determine the power distribution within the sampling volume; $|W|^2$ describes the power

204   distribution in range -in this model the function proposed by Doviak and Zrnic (1992) is used-

205   and f^4 varies with the angle from the center of the beam (and is approximated with a Gaussian

206   function).

207   Equation 2 considers the effect of the power distribution within the beam, the effect of

208   beam broadening, and path attenuation by precipitation. Each radar measurement is actually

209   obtained as the average of several pulses, and averaged to the final product resolution (1 km).

210   *3.3. Attenuation model*

211   The attenuation model is based in the assumption of a *k-Z* power law relationship ($k = \alpha \cdot$

212   Z^β). The model used here accounts for some spatial variability of the factor α of the *k-Z*

213   relationship according to Equation 3. Consequently, the *k-Z* relationship becomes $k(x, y, h) =$

214     $\alpha(x, y, h) \cdot z(x, y, h)^{\beta_0}$, where the parameter β_0 has been adjusted to *k* and *Z* for a sample of *Z*

215   values assuming a Marshall-Palmer drop size distribution (Marshall and Palmer, 1948).

$$\alpha(\mathbf{a}) = (a_1 x + a_2 y + a_3 h + a_4)^2 \qquad (3)$$

216   Note that the parameters $\mathbf{a} = (a_1, a_2, a_3, a_4)$ are control variables of the cost function, as

217   one can see in Equation 1; that is, they are optimized through the minimization instead of being

218   fixed a priori. The square on the right side of Equation 3 guarantees positive attenuation. Finally,

219   Equation 4 presents the equation for $\widetilde{K}(z, \mathbf{a}, r)$, the specific attenuation smoothed with the power

220   distribution of the beam:

$$\widetilde{K}(z, \mathbf{a}, r) = \frac{\int_{V(r)} |W|^2 f^4 \alpha(\mathbf{a}) z^{\beta_0} dV}{\int_{V(r)} |W|^2 f^4 \, dV} \qquad (4)$$

221   *3.4. Application of the inverse method*

222   The cost function (Equation 1) is minimized iteratively with the Conjugate Gradient method

223   (see e.g. Press et al., 1992) to retrieve the 3D composite. A first guess of the composite is needed

224   to initialize the minimization, as well as a first guess for the parameters $\mathbf{a}$ determining the *k-Z*

225   relationship. We have used as a first guess the composite obtained with the M2 technique

226   described in Section 2.2. As a first guess for the parameters $\mathbf{a}$ we have used those corresponding

10

227   to a uniform k-Z relationship $k = \alpha_0 \cdot Z^{\beta_0}$ for a Marshall-Palmer drop size distribution (see

228   Section 3.3), that is, $a_1 = a_2 = a_3 = 0$ and $a_4 = \sqrt{\alpha_0}$ (according to Equation 3).

4. Consistency of the inverse method in two case studies

230   The proposed inverse method has been applied for the first two rainfall cases presented in

231   Section 2.1. In this section, the retrieved fields are compared against those obtained with the two

232   methods described in Section 2.2 (M1 and M2).

233   *4.1. Case of 2006 UTC 17 September 2009*

234   The retrieved 3D reflectivity field [z in Equation 1] for this convective case is presented in

235   Figure 3. Figures 3a and 3b show that a good part of the domain is affected by precipitation,

236   including several convective cells embedded within widespread precipitation. The cell labeled as

237   A is an example of strong and deep convection near the LMI radar, while cell B is the largest of

238   the smaller cells around the CDV radar. Features with lower reflectivity values can be seen in the

239   southeastern portion of the domain. Several areas with no rain in the 2 km-CAPPI (Figure 3a)

240   show some reflectivity values between 25 and 35 dBZ in the 3 km-CAPPI (Figure 3b), indicating

241   overhanging precipitation (also visible in Figure 3c, near point P' and Figure 3d near point Q').

242   Vertical cross sections (Figures 3c and 3d) show the vertical development of convective cells A

243   and B (cell A reaches 6 km in height and cell B up to 5 km).

244   The 2-km CAPPIs obtained with the methods M1 and M2 are shown in Figures 4a and 4b.

245   Both fields show features similar to those observed in the composite obtained with the inverse

246   method (Figure 3a) but both are clearly smoother. Because the resolution of the observation grid

247   (1km x 1°) is lower than the grid spacing of the composites, the M1 and M2 composites

248   (obtained directly by from the observed reflectivity values) are smoother than the retrieval from

249   the inverse method. In addition, in the M2 case linear interpolations involved in the method (see

250   Section 2.2) contribute also to this fact. As expected, higher values can be seen all over the

11

251 domain in the M1 composite over the entire domain. In particular, in the area located north of
252 cell A, all values obtained with the M2 technique are obviously lower. In this area, values from
253 CDV radar are higher than the LMI values because observations from LMI radar are strongly
254 attenuated by intense rainfall near the radar; consequently, the M1 composite (based on choosing
255 the maximum value) is dominated by CDV values, while the M2 composite (built depending on
256 the distance) is influenced by values from both radars.

257 In the vertical cross sections showed in Figures 4c and 4d, we can see that the representation
258 of cell A is smoother than that obtained with the inverse method, and that method M2 produces
259 reflectivity values clearly lower (mainly because of the large attenuation of the observations of
260 LMI radar).

261 CAPPIs and vertical cross sections of the inverse method retrieval (Figure 3) show certain
262 level of noise at small scales, with no clear physical meaning, and probably an effect of the
263 numerical minimization. For example, we can see some scattered strong reflectivity around 2 km
264 altitude (Figure 3c and 3d). In the 3 km-CAPPI (Figure 3b), ring-shaped artifacts are visible in the
265 upper levels. This is because at this height observations are less dense and most of these grid
266 points are far from radar measurements. The ring shape patterns appear in the intersection areas
267 of the different PPIs (as can be checked with the thin lines represented in Figure 4).

268 Figure 5a shows the first PPI of actual observations recorded with the LMI radar (i.e. the
269 term $dB[Z_{LMI}]$ in Equation 1). The field has in general lower intensities than the retrieved
270 Cartesian field (z) at similar heights in Figure 3 (for instance, we can roughly identify cell B in
271 Figure 5a). The main reason is the effect of path attenuation due to the strong convective cell
272 near the LMI radar (present in the retrieval of Figure 3a). Similarly, this cell near the LMI radar is
273 no apparent in CDV observations (Figure 6a) because of the effect of path attenuation due to cell
274 A. Though, in general, CDV observations (Figure 6a) resemble more the fields at constant height
275 of Figure 3 and one can clearly identify cells A and B.

276   As explained in previous sections, the retrieved composites are expected to mitigate the

277   effects of known sources of error affecting the observations of individual radars. Consequently,

278   the retrieved mosaics cannot be directly compared with individual radar scans, where the effect of

279   errors such as beam broadening or path attenuation cannot be neglected. The way we have

280   chosen to address this aspect has been simulating the observations of each radar using the model

281   of Equations 2-4 to reflect the impact of the errors affecting individual radar observations. Once

282   a composite has been generated, a complete volumetric scan is simulated for each radar,

283   obtaining how radars would observe the obtained composite according to our model. Then the

284   simulations are compared against the actual observations.

285   Thus, to qualitatively assess the consistency of the proposed method, Figure 5d shows

286   simulated observations for the LMI radar corresponding to the 0.6°-PPI. These simulations have

287   been obtained by applying the observation operator for the LMI radar $dB[\tilde{Z}_{m,LMI}(\cdot)]$ over the

288   retrieved reflectivity field (z) using the simulation procedure described in Sections 3.2 and 3.3.

289   Simulations have similarly been obtained over the composites generated with the compositing

290   techniques M1 and M2 (Figures 5b and 5c, respectively). Visual comparison of Figures 5a and 5d

291   shows remarkable resemblance between observations and simulations for the LMI radar.

292   Simulations computed with the radar operator $dB[\tilde{Z}_{m,LMI}(\cdot)]$ over the M1-composite (Figure

293   5b) or over the M2 composite (Figure 5c) show clear discrepancies with respect to observations.

294   Similar results have been obtained for the CDV radar (shown in Figure 6). It is worth noting the

295   following features in Figures 5 and 6:

296   • The attenuation corridor in LMI observations (C in Figure 5a), is well reproduced in

297   the simulations performed over the retrieved field (Figure 5d).

298   • Convective cells labeled as A and B in CDV observations (Figure 6a) show lower

299   values in simulations performed over the M1 composite (Figure 6b). In the

300   simulation over the M2 composite (Figure 6c) reflectivities are even weaker. On the

13

301   other hand, convective cells A and B are quite well reproduced in the simulation over

302   the retrieved field (Figure 6d). Observed extreme values in A are not fully retrieved

303   perhaps due to the presence of hail, not considered in the simulation model.

304   • Figure 6c shows that M2 significantly underestimates reflectivities in the region

305   labeled as D, replicating the attenuation corridor C in LMI radar (Figure 5a). This is

306   due to the fact that M2 composites are based on a distance-weighted average, giving

307   more weight in this area to the attenuated LMI observations (closer to the LMI

308   radar). It should be noted that this method is designed for an S-band radar network

309   in which path attenuation in rain is not as significant as at C-band.

310   The resemblance between the simulations performed on the retrieved field and the

311 observations at the elevation of 0.6° confirms the compatibility of the retrieval with actual

312 observations from both radars as intended. That is, according to our observation model

313 expressed as the observation operator $dB[\tilde{Z}_{m,l}(\cdot)]$ (see Equations 1 and 2), the composite

314 retrieved with the numerical minimization is actually a good representation of the observed

315 rainfall field.

316   Scores of correlation, bias and root mean squared error (RMSE) are used to assess the

317 similarity between the observations and the simulations performed over the mosaics.

318 Observations cannot be directly compared with reflectivity composites because of the effects of

319 sources of error as path attenuation of beam broadening. Simulations over the obtained

320 composites include such effects according to our observation model and its similarity with

321 observations can be used as an indicator of the compatibility of the composited fields with

322 observations.

323   The left part of Table 2 shows that better results have been obtained with the proposed

324 inverse method than with the M1 and M2 techniques with the only exception of the bias for

325 CDV in comparison with the M1 technique. The inverse method is based on the minimization of

326   the cost function, which is the total of the squared errors, and this is directly related with the

327   RMSE of both radars. Thus the improvement in the RMSE basically reflects the consistency of

328   the method.

329   On the other hand, it is worth noting that the retrieved 3D field is implicitly corrected for

330   path attenuation which is included in the simulation procedure [see Equations 2, 3 and 4].

331   Equations 3 and 4 allow us to simulate path attenuation and use it to correct attenuated

332   observations. An example of such corrected observations is shown in Figure 7 together with the

333   simulated path integrated attenuation (PIA) fields. Once corrected for attenuation, the

334   observations of the two radars (Figures 7a and 7b) show more resemblance with each other; that

335   is, path attenuation explains a good part of the differences between the observed fields (Figures

336   5a and 6a). Figures 7c and 7d show that the simulated PIA reaches values up to 30 dB for the

337   LMI radar and up to 20 dB for the CDV radar.

338   The remaining differences between the observations of the two radars can, at least in part, be

339   explained by the differences in height of observations and beam broadening. The clearest

340   difference is in the region labeled as E, where LMI simulations show a region of intense

341   reflectivity (Figure 7a) that has no correspondence in the first PPI of CDV (Figure 7b). This

342   strong reflectivity values are only detected in high elevations (not shown) meaning that intense

343   rainfall does not reach the ground at this particular time.

344   *4.2. Case of 1430 UTC 4 February 2010*

345   The composite obtained for this case is shown in Figure 8. The 1.5-km and 2-km CAPPIs

346   (Figures 8a and 8b) show a uniform precipitation field, characteristic of a widespread situation.

347   The 2-km CAPPI shows higher reflectivity values than at 1.5 km because it approximately

348   corresponds to the height of the bright band peak. This can be confirmed with vertical cross

349   sections of the retrieved field (Figures 8c and 8d) and their mean VPR.

15

350   Simulations over the retrieved field reproduce remarkably well the observations, as shown in

351   Figure 9 for the LMI and CDV radars. In particular, the traces of the bright band are well defined

352   for both radars. The main difference is that for both radars the simulations are slightly smoother

353   than observations.

354   The scores presented in right part of Table 2 are presented to assess the compatibility of the

355   composites obtained with the different techniques (M1, M2 and the inverse method) with the

356   observations. In all cases, the scores of the composite obtained with the inverse method are

357   better for both radars.

358   In this case the path-integrated attenuation (PIA) does not exceed 4 dB in the rain region

359   (not shown) because of the moderate reflectivity values, and no attenuation is considered in the

360   snow region. In the melting snow region reflectivity values are considered as if were due to rain,

361   which results in higher PIA values. Few studies in the literature focus on the attenuation in

362   melting snow; among those, Bellon et al. (1997) found that the attenuation in the melting layer is

363   3-5 times the attenuation obtained as if the reflectivity values in the melting layer were due to rain

364   with an X-band radar at vertical incidence. If that was applicable for low-elevation C-band

365   measurements, our approach would underestimate the attenuation in the melting layer.

366   Results presented so far show the consistency of the inverse method at retrieving a

367   reflectivity field that is the most compatible with actual observations and the radar model, by

368   comparison with the observations of the radars involved in the composites. However, a proper

369   evaluation of the generated retrievals requires the use of independent information. The following

370   sections are, thus, devoted to the evaluation of the retrievals using two independent sources of

371   information: a third radar and a raingauge network.

372   **5. Comparison with the observations of an independent radar**

373   A quantitative evaluation of the composites is presented in this Section for an intense rainfall

374   event. Three-dimensional reflectivity composites have been retrieved using LMI and CDV

375   volume scans between 0000 and 1200 UTC of 2 November 2008. Every 30 minutes a composite

376   has been obtained with the M2 technique. This composite has been used as a first guess in the

377   iterative minimization of the inverse method (as introduced in Section 3.4). The proposed inverse

378   method is compared here against the M2 technique since the M1 methods had worse results in

379   the consistency analysis (see Table 2). The evaluation of the composites is based on the

380   comparison with the observations of the BAR radar, not used in the production of the mosaics.

381   Simulations of BAR observations have been computed over all composites and the similarity

382   between observations and simulations is quantified to assess the quality of the generated

383   composites.

384   *5.1. Case of 0330 UTC 2 November 2008*

385   This example corresponds to the volume scans recorded on 2 November 2008 at 0330 UTC.

386   Figure 10 shows the reflectivity field at 2 and 3 km in height, and vertical cross sections of the

387   composite obtained with the inverse method using LMI and CDV radar observations.

388   We can see that, at this time step, a good part of the domain is covered with rainfall and that

389   there are several embedded convective cells (Figures 10a and 10b). For instance, in the region

390   labeled as A, there is a convective cell with high values of reflectivity (up to 66 dBZ), that extends

391   to the north with zones of intense rainfall, but with less high values and lower vertical

392   development (Figure 10c). In Figure 10d, one can see the vertical development of the cell labeled

393   as B.

394   To analyze the performance of the compositing techniques, we compare actual BAR

395   observations with the BAR simulations performed over the retrieved composite using the model

396   that reproduces the radar sampling of the atmosphere (see Sections 3.2 and 3.3). Since BAR polar

397   observations are affected by path attenuation and beam broadening, it is necessary to simulate

398   these phenomena on the retrieved Cartesian composites to guarantee that we are comparing

399   values of the same nature (similarly as done in section 4). We can also carry out this comparison

17

400   with the radars involved in the composition (LMI and CDV), as a way to confirm the consistency

401   of the method shown in previous sections.

402   Observations and simulations for the first elevation of the BAR radar are shown in Figure

403   11. There is a region in the southeast not included in the comparison domain (shaded area in

404   observation and gray area in simulations); it corresponds to observations of the BAR radar where

405   the simulation is not possible due to the lack of observations from the other two radars. In this

406   region BAR observations are lower in height than the LMI and CDV coverage [note that the

407   BAR radar is located at a lower altitude (663 m) than LMI and CDV radars (910 m and 825 m,

408   respectively)].

409   We can see that in the M2 simulation (Figure 11b), the convective cell B takes lower values

410   than observed (Figure 11a), and the same happens in the attenuation corridor behind; in the

411   simulation over the composite obtained with the inverse method, both the cell and the

412   attenuation corridor resemble more the observed ones. Thus, there is a qualitative improvement

413   in the BAR simulations derived from the inverse method composite.

414   To quantify the similarity between observations and simulations, the left part of Table 3

415   shows the values of correlation, bias and root mean squared error (RMSE) for the first elevation

416   of the BAR radar, i.e. for the fields showed above (Figure 5). The results of the evaluation using

417   the observations of the BAR radar as reference are quite similar for both techniques in terms of

418   the obtained scores; the inverse method has only slightly better results than the M2 technique

419   despite of the qualitative improvement shown in Figure 5. The right part of Table 3 presents the

420   values of the same scores calculated using all the PPIs of the BAR radar, and we can also see

421   similar results for both techniques.

422   *5.2. Scores*

423   Bias, correlation and RMSE computed from the comparison between observations and

424   simulations for the BAR radar have been calculated for all the composites in the evaluation

18

425   period. Top panels of Figure 12 show the evolution of the bias in the period for the three radars

426   and both compositing techniques (M2 and the inverse method). The bias for the BAR radar

427   (Figure 12c) is quite similar for both techniques in most of the cases, and in some of them the

428   bias is better for the inverse method than for the M2 technique. Note that the composite

429   retrieved at a given time step only uses information from this particular time step; so the scores

430   of consecutive time steps are unrelated except for that original observations are consecutive. The

431   values of the RMSE for the BAR radar (Figure 12f) are again very similar for both techniques but

432   in some cases we obtain slightly worse results with the inverse method. In Figure 12i we can see

433   that the correlation between observations and simulations is quite high in all cases. Similarly as

434   for the RMSE, for the independent radar BAR, the M2 technique produces equal or better

435   correlation values than the inverse method.

436   Summarizing, the results of Figure 12 show a small gain of the inverse method in the bias,

437   but in terms of RMSE and correlation, the results are very similar as the M2 technique. For the

438   radars involved in the composites (LMI and CDV), the scores of the inverse method are better,

439   confirming the consistency of the method. In some time steps, as 0100 UTC, the minimization

440   process of the inverse method found a minimum near the first guess (which is the M2-

441   composite) and so the difference between the scores of both techniques is very small.

442   *5.3. Reflectivity distributions*

443   The reflectivity distributions corresponding to the first elevation for the entire evaluation

444   period are shown in top panels of Figure 13. The distribution of reflectivity values obtained with

445   the inverse method for the BAR radar is very similar to the one obtained from observations while

446   the M2 technique underestimates the frequency of high values (greater than 40 dBZ).

447   *5.4. Scale analysis*

448   In this Section, the radially-averaged Fourier spectra of the reflectivity fields are used to

449   assess how the simulations over the mosaics obtained with the different techniques reproduce the

450   spatial variability of observations [as done, for instance, by Pegram et al. (2011)]. To highlight the

451   discrepancies between the spectra of observations and simulations, bottom panels of Figure 13

452   shows the ratio between the mean spectra of the simulated and observed reflectivity fields. For

453   the BAR radar, the representation of scales between 2 and 10 km is less underestimated with the

454   inverse method; and the contribution of smaller scales (less than 2 km) is overestimated in the

455   inverse method simulations, while it is underestimated in the M2 simulations.

456   If we focus on the scales of convective storms, between 2 and 20 km [corresponding to the

457   meso-γ scale following the classification of Orlanski (1975)], we can see that the inverse method

458   reproduces the contribution of those scales better than the M2 technique.

6. Comparison with raingauges

460   This Section presents an evaluation of compositing techniques in terms of accumulated rain.

461   The 2-km CAPPI of the composites has been used as an estimation of rainfall at ground every 6

462   minutes. The reflectivity fields have been transformed into rain-rate and accumulated for the

463   analyzed 12 hours period assuming that between one time step and the next one the precipitation

464   fields moves at constant velocity and that rain intensity varies linearly (as in Fabry et al. 1994).

465   Estimated values at raingauge locations have been compared against the actual raingauge

466   observations. The same comparison has been carried out using the 2-km CAPPIs of individual

467   radars (LMI and CDV). These raingauges belong to the networks of the Catalan Water Agency

468   (ACA) and SMC and their records are routinely quality controlled.

469   Figure 14 shows the accumulation maps obtained from the different mosaics and individual

470   radars. An almost South-North band of values above 35 mm can be seen in accumulations,

471   indicating the location of strong convective cells in the analyzed period.

472   In Figure 15 we can see that the estimates from individual radars (first row) show a good

473   agreement with the low values registered with raingauges, while high values have been

474   underestimated probably because of the significant path attenuation observed in individual PPIs.

475   The composites obtained with the M1 technique results in a general overestimation except for

476   the extreme values (Figure 15 second row, left panel). Contrarily, the comparison of the M2-

477   composite against raingauges shows a general underestimation for values greater than 40 mm

478   resulting in a bias higher than obtained for individual radars (see Figure 15, second row, right

479   panel). The scatterplot for the inverse method (Figure 15, third row) shows better results than

480   M1 and M2. There is a good agreement in the low values as found for individual radars (instead

481   of the overestimation obtained for M1), and a general improvement with respect to the M2

482   technique, especially in the reproduction of the high values. The bias (and to a lesser extent the

483   RMSE) has been reduced in comparison with the rest of the techniques.

484   **7. Conclusions and discussion**

485   A methodology for obtaining 3D reflectivity composites using measurements from several

486   radars is presented. The proposed inverse method is based on retrieving the 3D Cartesian

487   reflectivity field most compatible with the available radar observations assuming the models for

488   the radar sampling of the atmosphere and path attenuation (Sections 3.2 and 3.3). The retrieved

489   fields reproduce coherent features such as the vertical development of convective cells or the

490   reflectivity enhancement of the bright band, as shown for two significantly different examples.

491   The compatibility of the composites with actual observations has been assessed through a

492   simulation model of the radar sampling of the atmosphere. From the retrieved composite,, a

493   complete volumetric scan is simulated for each radar, considering how radars would observe it

494   according to our model. Then the simulations are compared against the actual observations. In

495   the observation-simulation comparison for the radars involved in the composition process (LMI

496   and CDV), the inverse method gets better results for the evaluation period in terms of scores,

21

497 reflectivity distribution and scale analysis, confirming the consistency of the method. Note that

498 while the cost function minimized by the inverse method (total of squared differences) is directly

499 related with the RMSE, the relationship of this function with correlation, bias, reflectivity

500 distribution or the Fourier spectra is more indirect (so better results in these aspects could be

501 more relevant).

502   A quantitative evaluation involving two independent sources of information, a radar and a

503 raingauge network, has been carried out to compare the inverse method against an existing

504 technique based on a distance-weighted mean (M2). The raingauge network in the area provides

505 direct measurements of rainfall at ground level, while independent radar observations allow us to

506 evaluate the 3D reflectivity composites.

507   The comparison of the retrieved mosaics with actual radar observations requires the

508 simulation of radar observations using the radar sampling model. This allows us to account for

509 the errors affecting radar PPIs. The analyzed techniques obtain similar results when comparing

510 the BAR observations and simulations in terms of bias, correlation and RMSE. However, the

511 analysis of the distribution of reflectivity values shows that the M2 technique underestimates

512 systematically the presence of high values, while the inverse method tends to better reproduce the

513 upper tail of the distribution. In the scale analysis the inverse method reproduces the

514 contribution of the scales between 2 and 20 km better than the M2 technique; with respect to the

515 smaller scales, the fields obtained with the inverse method are too noisy, while the M2 fields tend

516 to be too smooth (which is not surprising, as the technique is based on a distance-weighted

517 mean). It is worth noting that the smoothness of M2 fields contributes to the good results in

518 terms of RMSE for this technique, while the inverse method obtains similar RMSE values while

519 reproducing better the variability of the field and capturing better the high reflectivity values.

520   On the other side, values of accumulated rainfall obtained with the different compositing

521 techniques have been compared against the available raingauge records. The combined use of

522   observations from two different radars with the inverse method is shown to be better than each

523   of these radars separately. The inverse method accumulation also compares better with raingauge

524   amounts than both M1 and M2 techniques. The M1 technique overestimates most of the

525   raingauge values while the M2 technique suffers from general underestimation.

526   The method proposed in this work implicitly corrects for attenuation. The simulation

527   procedure accounts for attenuation and is inverted using network information as a constraint to

528   avoid the instabilities of the attenuation correction by intense rainfall. This is a feature that the

529   M2 technique does not have (it was originally designed for S-band radars). It allows the inverse

530   method to capture better the high reflectivity values as we see in the reflectivity distributions and

531   in the comparison with raingauge measurements. This fact, together with the better reproduction

532   of the scales associated with convective cells, show the advancement of the inverse method with

533   respect to the M2 technique.

534   The temporal localization of the reflectivity measurements is a source of error in the

535   composition of observations from different radars. The time spent in the radar scanning of the

536   atmosphere is relevant when constructing a high-resolution composite assigned to a particular

537   instant. It is also relevant that two different radars will rarely take measurements at the same

538   location at the same time [Lakshmanan et al. (2006) and Langston et al. (2007) consider this fact

539   in a weighted mean approach, giving greater weights to the more recent measurements]. Here we

540   have tried to partially compensate for these temporal differences by shifting the observations

541   with the estimated motion fields. The inverse method is more susceptible to be affected by these

542   synchronization errors and their propagation in the simulations than the M2 technique, thanks to

543   the smoothing effect of M2.

544   The problem of retrieving reflectivities along the path of a radar beam from attenuated

545   values is known to be underdetermined and very sensitive to small errors [see e.g. Hitschfeld and

546   Bordan (1954), Haddad et al. (1995) or Berne and Uijlenhoet (2006)]. In our approach, the use of

23

547 multiple observations is chosen to constrain the inversion of the problem and to reduce the

548 degrees of freedom. However, it needs to be noticed that, whereas in the lower parts of the

549 domain (well covered with the lower PPIs from both radars) the problem is now better

550 constrained, the regions near the top of the domain are still sparsely sampled, and the problem is

551 clearly underdetermined. Similarly, the proposed methodology would suffer from

552 underdetermination in larger domains where only measurements of one radar are available. These

553 facts restrict its applicability to overlapping regions in dense radar networks, and the extension to

554 areas with single-radar observation would need to use other methods.

555 At the present stage, the high computational cost of the method is a limitation for its

556 application in real-time over large domains covered with dense radar networks. Therefore, the

557 selection of the grid spacing needs to balance factors such as the number of unknowns (which

558 determines the number of degrees of freedom of the problem) and the computational cost, but

559 should enable realistic simulation of the radar sampling of the atmosphere (which requires a

560 relatively dense grid). Thus, the grid spacing of 500 x 500 x 250 m^3 has been chosen as a

561 compromise between these factors given the range resolution of observations (1 km).

562 The inverse method approach provides a flexible framework that allows further

563 improvements in the 3D reflectivity retrieval such as:

564 - The cost function is chosen here as a simple approach to quantify the discrepancies

565 between simulations and observations. In particular, the quality of each observation

566 is equally weighted, neglecting the differences in the quality of the observations (e.g.

567 its well known dependence with range) and the spatial correlation of observation

568 errors [see e.g. Vignal et al. (2003) or Berenguer and Zawadzki (2008)]. In this sense,

569 the cost function allows including the information of the estimated observation error

570 covariance matrices, which would make the solution optimal in a least squares sense

571 [see e.g. Kalnay (2003)].

572   • The methodology can be easily generalized to any number of available radars by
573   simply extending the cost function with additional terms.

574   • The retrieved fields show too much variability for small scales. This fact could be
575   mitigated by extending the formulation of the cost function. The smoothness of the
576   retrieved composites can be imposed adding a smoothing constraint in the cost
577   function, as proposed by Ebtehaj and Foufoula-Georgiou (2012). An example of this
578   is the term J_2 in Laroche and Zawadzki (1995) applied to the retrieval of wind fields.

579   • The attenuation model is based on a simple parameterization of the factor   of the
580   k-Z relationship to allow for some spatial variation of this relationship. Although this
581   model only accounts for part of the real variability of the drop size distribution, the
582   inverse method is ready to introduce further refinements in the attenuation model,
583   for instance to distinguish different precipitation regions (convective or stratiform
584   rain, snow…) based on original observations. In addition, in dual-polarization radars,
585   the use of observations of differential phase, Φ_{DP} could be an interesting alternative
586   to further constrain the retrieval by minimizing the departures from the relationships
587   between Φ_{DP} and the PIA (e.g. Park et al., 2005; Cao et al., 2013).

588   • With the results presented here, it seems advisable to work on a hybrid technique
589   that uses the inverse method in certain regions (specially those affected by high
590   reflectivity values and/or significant path attenuation) and the M2 technique
591   elsewhere. In this manner, we would benefit from (i) the strengths of the inverse
592   method where its contribution is more evident, and (ii) a reduction of the
593   computational cost using the M2 method, while maintain a good performance as
594   guaranteed by its low RMSE in the areas not affected by severe attenuation.

595   The performance of the proposed technique has been demonstrated in this paper for a single
596   12-hour event. A comprehensive evaluation over a larger number of events would be necessary

597 to make the findings presented here more conclusive. Finally, the formulation of the inverse

598 method calls for a sensitivity analysis using a known 3D reflectivity field (either synthetic or

599 based on simulations –for example, obtained with a high-resolution NWP model-). One can

600 simulate the observations from different radars and then apply the inverse method for

601 verification [similarly to what is done by Chandrasekar and Lim (2008)]. The fact of knowing the

602 initial reflectivity field would allow us to study the effect of the number of radars, or different

603 perturbations of the simulations.

Acknowledgements

612

References

Andrieu, H., Creutin, J.D., 1995. Identification of Vertical Profiles of Radar Reflectivity for Hydrological Applications Using an Inverse Method. Part I: Formulation. J. Appl. Meteorol., 34(1): 225-239.

Bech, J. et al., 2011. A Mediterranean nocturnal heavy rainfall and tornadic event. Part I: Overview, damage survey and radar analysis. Atmos. Res., 100(4): 621-637.

Bellon, A., Lee, G., Zawadzki, I., 2005. Error Statistics of VPR Corrections in Stratiform Precipitation. J. Appl. Meteorol., 44(7): 998-1015.

Bellon, A., Zawadzki, I., Fabry, F., 1997. Measurements of melting layer attenuation at X-band frequencies. Radio Sci., 32(3): 943-955.

Berenguer, M., Sempere-Torres, D., Corral, C., Sánchez-Diezma, R., 2006. A Fuzzy Logic Technique for Identifying Nonprecipitating Echoes in Radar Scans. J. Atmos. Ocean.Technol., 23(9): 1157-1180.

Berenguer, M., Zawadzki, I., 2008. A Study of the Error Covariance Matrix of Radar Rainfall Estimates in Stratiform Rain. Weather Forecast., 23(6): 1085-1101.

Berenguer, M., Zawadzki, I., 2009. A Study of the Error Covariance Matrix of Radar Rainfall Estimates in Stratiform Rain. Part II: Scale dependence. Weather Forecast., 24: 800-811.

Berenguer, M., Sempere-Torres, D., and Pegram, G. G. S.: SBMcast - An ensemble nowcasting technique to assess the uncertainty in rainfall forecasts by Lagrangian extrapolation, Journal of Hydrology, 404, 226-240, 2011.

27

633 Berne, A., Uijlenhoet, R., 2006. Quantitative analysis of X-band weather radar attenuation

634 correction accuracy. Nat. Hazard. Earth Syst. Sci., 6(3): 419-425.

635 Cao, Q., Zhang, G., Xue, M., 2013. A Variational Approach for Retrieving Raindrop Size

636 Distribution from Polarimetric Radar Measurements in the Presence of Attenuation. J. Appl.

637 Meteorol. Climatol., 52(1): 169-185.

638 Chandrasekar, V., Lim, S., 2008. Retrieval of Reflectivity in a Networked Radar Environment. J.

639 Atmos. Ocean.Technol., 25(10): 1755-1767.

640 Delrieu, G., Creutin, J.D., Andrieu, H., 1995. Simulation of Radar Mountain Returns Using a

641 Digitized Terrain Model. J. Atmos. Ocean.Technol., 12(5): 1038-1049.

642 Delrieu, G., Ducrocq, V., Gaume, E., Nicol, J., Payrastre, O., Yates, E., Kirstetter, P. E., Andrieu,

643 H., Ayral, P. A., Bouvier, C., Creutin, J. D., Livet, M., Anquetin, S., Lang, M., Neppel, L., Obled,

644 C., Parent-du-Chatelet, J., Saulnier, G. M., Walpersdorf, A., and Wobrock, W., 2005. The

645 catastrophic flash-flood event of 8-9 September 2002 in the Gard region, France: A first case

646 study for the Cevennes-Vivarais Mediterranean Hydrometeorological Observatory, J. Hydromet.,

647 6: 34-52.

648 Doviak, R.J., Zrnic, D.S., 1992. Doppler radar and weather observations. Academic Press, 562

649 pp.

650 Ebtehaj, A.M., Foufoula-Georgiou, E., 2012. Variational downscaling, data fusion and

651 assimilation of hydro-meteorological states via regularized estimation. Water Resour. Res.:

652 Accepted.

653 Fabry, F., Bellon, A., Duncan, M.R., Austin, G.L., 1994. High resolution rainfall measurements

654 by radar for very small basins: the sampling problem reexamined. J. Hydrol., 161(1-4): 415-428.

28

655   Fornasiero, A., Alberoni, P.P., Amorati, R., Marsigli, C., 2006. Improving the radar data

656   mosaicking procedure by means of a quality descriptor, Fourth European Conference on Radar

657   in Meteorology and Hydrology, Barcelona, Spain, pp. 378-381.

658   Haddad, Z.S., Im, E., Durden, S.L., 1995. Intrinsic Ambiguities in the Retrieval of Rain Rates

659   from Radar Returns at Attenuating Wavelengths. J. Appl. Meteorol., 34(12): 2667-2679.

660   Hitschfeld, W., Bordan, J., 1954. Errors inherent in the radar measurement of rainfall at

661   attenuating wavelengths. J. Atmos. Sci., 11(1): 58-67.

662   Kabèche, A., Testud, J., 1995. Stereoradar Meteorology: A New Unified Approach to Process

663   Data from Airborne or Ground-Based Meteorological Radars. J. Atmos. Ocean.Technol., 12(4):

664   783-799.

665   Kalnay, E., 2003. Atmospheric modeling, data assimilation and predictability. Cambridge

666   University Press, 341 pp.

667   Langston, C., Zhang, J., Howard, K., 2007. Four-Dimensional Dynamic Radar Mosaic. J. Atmos.

668   Ocean.Technol., 24(5): 776-790.

669   Lakshmanan, V., Smith, T., Hondl, K., Stumpf, G.J., Witt, A., 2006. A Real-Time, Three-

670   Dimensional, Rapidly Updating, Heterogeneous Radar Merger Technique for Reflectivity,

671   Velocity, and Derived Products. Weather Forecast., 21(5): 802-823.

672   Laroche, S., Zawadzki, I., 1995. Retrievals of Horizontal Winds from Single-Doppler Clear-Air

673   Data by Methods of Cross Correlation and Variational Analysis. J. Atmos. Ocean.Technol., 12(4):

674   721-738.

675   Marshall, J.S., Palmer, W.M.K., 1948. The distribution of raindrops with size. J. Meteorol., 5(4):

676   165-166.

677   Menke, W., 1989. Geophysical Data Analysis: Discrete Inverse Theory. Academic Press, 260 pp.

678   Michelson, D.B. et al., 2000. BALTEX radar data centre products and their methodologies.

679   SMHI reports meteorology and climatology. Swedish Meteorological and Hydrological Institute,

680   76 pp.

681   Orlanski, I., 1975. A rational subdivision of scales for atmospheric processes. Bull. Am. Meteorol.

682   Soc., 56(5): 527-530.

683   Park, S.G., Bringi, V.N., Chandrasekar, V., Maki, M., Iwanami, K., 2005. Correction of Radar

684   Reflectivity and Differential Reflectivity for Rain Attenuation at X Band. Part I: Theoretical and

685   Empirical Basis. J. Atmos. Ocean.Technol., 22(11): 1621-1632.

686   Pegram, G., Llort, X., Sempere-Torres, D., 2011. Radar rainfall: Separating signal and noise fields

687   to generate meaningful ensembles. Atmos. Res., 100(2-3): 226-236.

688   Peura, M., 2010. The living composite, Sixth European Conference on Radar in Meteorology and

689   Hydrology (ERAD), Sibiu, Romania.

690   Peura, M., Koistinen, J., 2007. Using radar data quality in computing composites and nowcasting

691   products, 33rd Conference on Radar Meteorology. American Meteorological Society, Cairns,

692   Australia.

693   Press, W.H., Teukolsky, S.A., Vetterling, W.T., Flannery, B.P., 1992. Numerical Recipes in C: The

694   Art of Scientific Computing. Cambridge University Press, 1035 pp.

695   Roca-Sancho, J., Berenguer, M., Sempere-Torres, D., 2013. An inverse method to retrieve 3D

696   radar reflectivity composites. Part II: Evaluation. J. Hydrol.: Submitted.

697   Sánchez-Diezma, R., 2001. Optimization of rainfall measurements with weather radars for

698   hydrologic applications (in spanish). Ph.D. Thesis Thesis, Universitat Politècnica de Catalunya,

699   313 pp.

700   SMC, 2009. Monthly Weather Bulletin. September 2009 (in catalan). Servei Meteorològic de

701   Catalunya, Departament de Medi Ambient i Habitatge, Generalitat de Catalunya.

702   Srivastava, R.C., Tian, L., 1996. Measurement of Attenuation by a Dual-Radar Method: Concept

703   and Error Analysis. J. Atmos. Ocean.Technol., 13(5): 937-947.

704   Tabary, P., Frech, M., Dempsey, P., 2009. OPERA III. Evaluation of new technologies.

705   EUMETNET.

706   Testud, J., Amayenc, P., 1989. Stereoradar Meteorology: A Promising Technique for observation

707   of Precipitation from a Mobile Platform. J. Atmos. Ocean.Technol., 6(1): 89-108.

708   Trapp, R.J., Doswell, C.A., 2000. Radar Data Objective Analysis. J. Atmos. Ocean.Technol.,

709   17(2): 105-120.

710   Vignal, B., Andrieu, H., Delrieu, G., Creutin, J.D., 2003. Identification of Rain-Rate Profiles from

711   Radar Returns at Attenuating Wavelengths Using an Inverse Method: A Feasibility Study. J. Appl.

712   Meteorol., 42(7): 1014-1030.

713   Villarini, G., Krajewski, W., 2010. Review of the Different Sources of Uncertainty in Single

714   Polarization Radar-Based Estimates of Rainfall. Surv. Geophys., 31(1): 107-129.

715   Zawadzki, I., 1984. Factors affecting the precision of radar measurement of rain, 22nd

716   International Conference on Radar Meteorology. Amer. Meteor. Soc. 251-256, Zurich,

717   Switzerland.

718   Zhang, J., Howard, K., Gourley, J.J., 2005. Constructing Three-Dimensional Multiple-Radar

719   Reflectivity Mosaics: Examples of Convective Storms and Stratiform Rain Echoes. J. Atmos.

720   Ocean.Technol., 22(1): 30-42.

721

722

723

Figure 1. Illustration of radar locations and domain. Locations of La Miranda (LMI) radar, Creu del Vent (CDV) radar and Barcelona (BAR) radar are shown in a topographical map of NE Spain (near the city of Barcelona). Distances between radars are indicated. A square indicates the area covered by the 3D domain in which the composites are carried out. The dashed line indicated the extension of the domain needed to include the BAR radar.

Figure 2. Example of reflectivity composite with the maximum value technique. Vertical cross section of the reflectivity field obtained by the nearest neighbor algorithm for LMI (a) and CDV (b) radar observations for the 17 September 2009 2006 UTC. Thin lines represent the path of the center of the radar beam for each radar. Same vertical cross section of the reflectivity composite with the maximum value technique (c). Paths of the beams of both radars are represented in the latter. White means no rain. Gray areas correspond to regions without radar observations (in altitudes below 1 km) or without retrieved values (in higher altitudes). In region labeled as A the field obtained by the maximum value technique is dominated by the CDV radar, while in region labeled as B LMI radar is dominant.

Figure 3. CAPPIs (Constant Altitude Plan Position Indicator) and vertical cross sections of the 3D reflectivity composite retrieved with the inverse method from radar observations measured at 2006 UTC on 17 September 2009. The CAPPIs correspond to heights of 2 and 3 km [(a) and (b) respectively] and vertical cross sections (c,d) are indicated in the CAPPIs with straight lines, line P-P' for x=17 km (c) and line Q-Q' for y=38.50 km (f). The thin lines on the panels correspond to the path of the radar ray for each elevation. Gray areas correspond to regions without radar observations (in altitudes below 1 km) or without retrieved values (in higher altitudes). A and B indicate two intense convective cells (see the text for further detail).

Figure 4. CAPPIs of the 3D reflectivity composite retrieved with the M1 (a) and the M2 technique (b) from radar observations measured at 2006 UTC on 17 September 2009 with the LMI and CDV radars. Vertical cross sections at x = 17 km of the M1 and M2 mosaics are shown in (c) and (d) respectively. The thin lines on the panels correspond to the path of the radar ray for each elevation. Gray areas correspond to regions without radar observations (in altitudes below 1 km) or without retrieved values (in higher altitudes). A and B indicate two intense convective cells.

Figure 5. Reflectivity field of the 0.6° elevation observed with the LMI radar on 17 September 2009 at 2006 UTC (a) and reflectivity fields corresponding to the simulation of the 0.6° elevation for the LMI radar over the fields obtained with the technique M1 (b), M2 (c) and the inverse method (d). LMI radar location is indicated with a star. White means no rain. Shaded areas in the

observation and gray areas in simulations are not included in the domain. Coordinate axis indicate Easting (x) and Northing (y) distance to the radar. Region C shows an attenuation corridor (a) that is quite better reproduced in (d) than in (b) or (c).

Figure 6. Reflectivity field observed with the CDV radar at 0.6º elevation on 17 September 2009 at 2006 UTC (a) and reflectivity fields corresponding to simulated observations at the same elevation over the composites obtained with the techniques M1 (b), M2 (c) and the inverse method (d). CDV radar location is indicated with a white star. Shaded areas in the observation and gray areas in the simulation are regions not included in the domain. Labels A and B indicate convective cells (see text for further detail). Label D shows underestimation due to the effect of the attenuation corridor in the LMI observation on the distance-weighted composite.

Figure 7. Example of observations corrected for attenuation. (a) Reflectivity field corresponding to the 0.6º elevation of the LMI radar. (b) Reflectivity field corresponding to the 0.6º of the CDV radar. (c,d) PIA fields corresponding to the reflectivity fields (a) and (b) respectively. Radar locations are indicated with white stars. White means no rain. Gray areas are not included in the domain. Coordinate axis indicate Easting (x) and Northing (y) distance to the radar.

Figure 8. CAPPIs and vertical cross sections of the 3D reflectivity composite retrieved with the inverse method from radar observations measured at 1430 UTC on 4 February 2010. The CAPPIs correspond to heights of 1.5 and 2 km [(a) and (b) respectively] and lines P-P' and Q-Q' indicate the vertical cross sections shown in (c) for x=20 km and (d) for y=50 km respectively. On the right of the vertical cross sections is the mean vertical profile of relectivity (VPR) of the corresponding vertical cross section, that is, for each height the mean reflectivity value of the cross section is represented. The thin lines on the panels correspond to the path of the center of the radar beam for each elevation. White means no rain. Gray areas correspond to regions without radar observations (in altitudes below 1 km) or without retrieved values (in higher altitudes).

Figure 9. Reflectivity fields recorded with the LMI radar (a) and CDV radar (b) on 4 February 2010 at 1430 UTC corresponding to elevations of 3º and 4º respectively. Reflectivity fields corresponding to simulations over the composite retrieved with the inverse method for the same radar and elevations are shown in (c) and (d). Location of radars is indicated with a star. White means no rain. Shaded areas in the observations and gray areas in the simulations are not included in the domain.

Figure 10. CAPPIs (Constant Altitude Plan Position Indicator) and vertical cross sections of the 3D reflectivity composite obtained with the inverse method using observations recorded with the

LMI and CDV radars the 2 November 2008 at 0330 UTC. The CAPPIs correspond to the heights of 2 and 3 km [(a) and (b) respectively] and the vertical cross sections are indicated in the CAPPIs with straight lines, line P-P' for x = 17 km (c) and line Q-Q' for y = 38 km (d). The thin lines represent the path of the radar beam for each elevation. The grey areas correspond to regions without radar observations (in altitudes below 1 km) o without retrieved values (in higher altitudes). A and B indicate two intense convective cells (see text for further detail).

Figure 11. Reflectivity field of the 0.5° elevation observed with the BAR radar on 2 November 2008 at 0330 UTC (a) and reflectivity fields corresponding to the simulation of the 0.5° elevation for the BAR radar over the fields obtained with the technique M2 (b) and the inverse method (d). BAR radar location is indicated with a star. White means no rain. Shaded areas in the observation and gray areas in simulations are not included in the domain.

Figure 12. Bias, correlation and RMSE (top to bottom) between observations and simulations over composites along the evaluation period for each compositing technique (M2 black line, inverse method red line) and for each radar (from left to right: CDV, LMI, BAR).

Figure 13. Top panels: Reflectivity distributions of the first elevation of the radar observations (black lines; from left to right: CDV, LMI, BAR) together with the reflectivity distribution of the corresponding simulations over the composites obtained with the M2 technique (blue lines) and with the inverse method (red lines). The used sample is the whole evaluation period (0000 UTC – 1200 UTC 2 November 2008). Bottom panels: Ratios of the mean 1D Fourier spectra of the reflectivity fields (observation, simulation derived from M2 technique and simulation derived from the inverse method) respect the mean 1D Fourier spectra of the observations over the evaluation period (black, blue and red lines respectively). The fields corresponding to the first elevation of each radar (from left to right: CDV, LMI, BAR) are used. The ratio between the average variance of the fields and the average variance of the observed fields is also shown.

Figure 14. Rain accumulation fields obtained with individual radars (first row) and three compositing techniques (second and third rows). Raingauge values are indicated in circles filled using the same color scale.

Figure 15. Scatterplots of the 12h-rain accumulation values obtained with individual radars (first row) and three compositing techniques (second and third rows) against raingauge values. The thin line is the 1:1 line indicating the position of identical values in raingauges and composites.

3

Name	La Miranda (LMI)	Creu del Vent (CDV)	Barcelona (BAR)
Wavelenght	5.3 cm	5.3 cm	5.3 cm
Pulse length	5 μs	5 μs	2 μs
Beam width (3-dB)	1.1°	1.1°	0.9°
Azimuthal resolution	1°	1°	0.8°
Radial resolution	1 km	1 km	1 km
Maximum range	130 km	150 km	120 km
Number of elevations	16	16	19
Lowest elevation	0.6°	0.6°	0.5°
Height	910 m	825 m	663 m
Temporal resolution	6 min	6 min	10 min

Table 1. Main characteristics of the three C-band radars used in this study.

2006 UTC 17 September 2009				1430 UTC 4 February 2010		
	Correlation	Bias [dB]	RMSE [dB]		Correlation	Bias [dB]	RMSE [dB]
LMI Radar				**LMI Radar**			
M1	0.91	1.92	6.33	**M1**	0.94	0.94	2.76
M2	0.95	0.31	4.45	**M2**	0.93	-0.96	3.22
Inverse method	0.98	0.05	3.00	**Inverse method**	0.97	-0.11	1.91
CDV Radar				**CDV Radar**			
M1	0.95	0.14	4.31	**M1**	0.89	4.53	5.70
M2	0.96	-2.11	4.57	**M2**	0.95	0.81	2.49
Inverse method	0.98	-0.39	2.72	**Inverse method**	0.98	0.01	1.58

Table 1. Scores of performance of different compositing techniques (M1, M2 and inverse method). Correlation, bias and root mean squared error (RMSE) between simulations and observations have been computed using all elevations. On the left the case of 17 September 2009 at 2006 UTC is assessed and the right side correspond to the case of 1430 UTC 4 February 2010. Top rows show the statistics for the LMI radar and bottom rows for the CDV radar.

1

2 November 2008 0330 UTC							
First elevation				**All elevations**			
	Correlation	**Bias [dB]**	**RMSE [dB]**		**Correlation**	**Bias [dB]**	**RMSE [dB]**
M2	0.94	-0.21	5.28	**M2**	0.93	0.10	4.61
Inverse method	0.95	0.06	4.71	**Inverse method**	0.94	0.13	4.45

Table 1. Scores of performance of the two compositing techniques (M2 and inverse method). Correlation, bias and root mean squared error (RMSE) between simulations and observations have been computed using only the first elevation (left-hand side) and all elevations (right-hand side) of the BAR radar. These values correspond to the case of 0330 UTC 2 November 2008.

Figure 1

Text labels in figure: CDV, BAR, Barcelona, LMI, 45 km, 72 km, 90 km
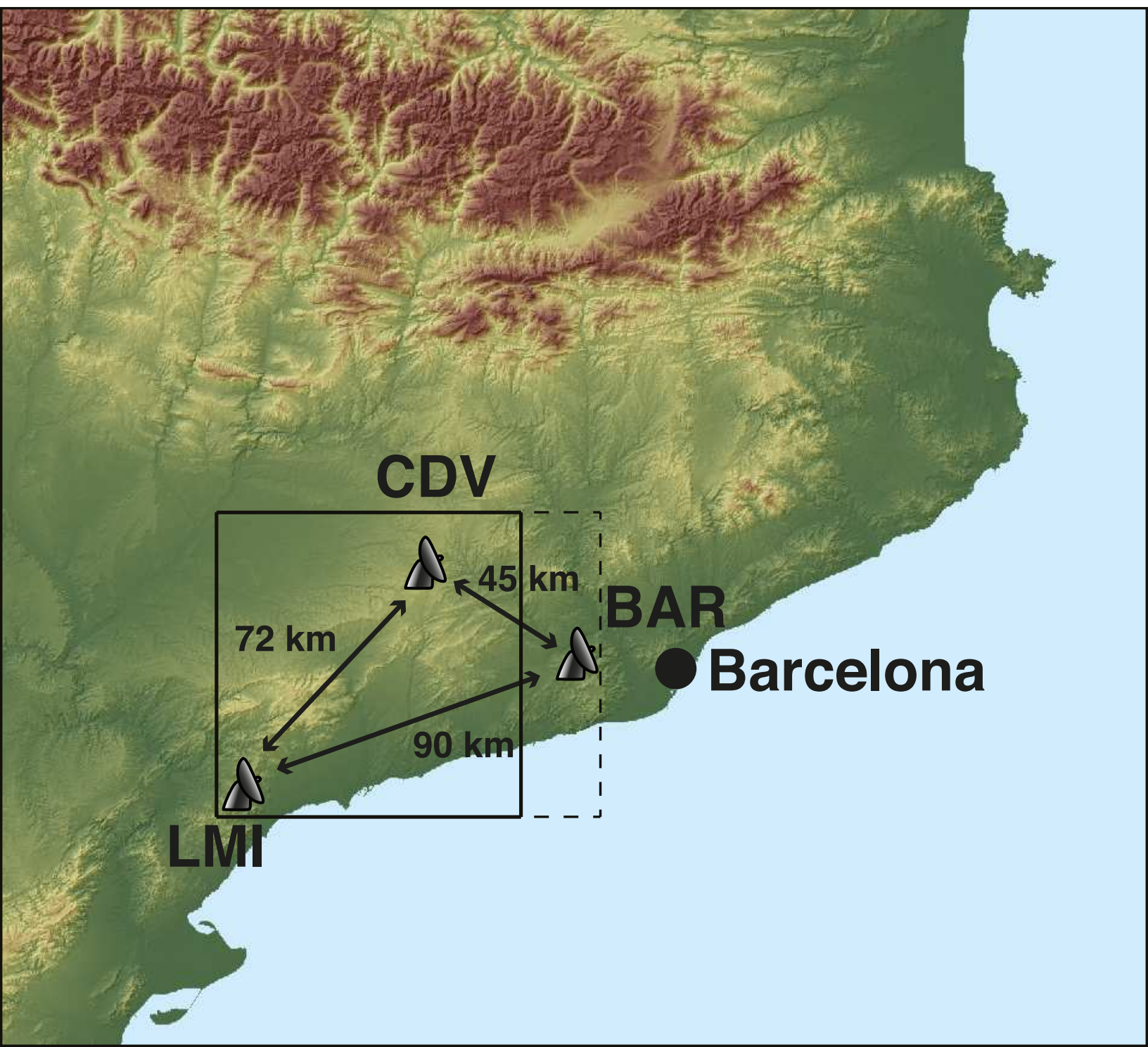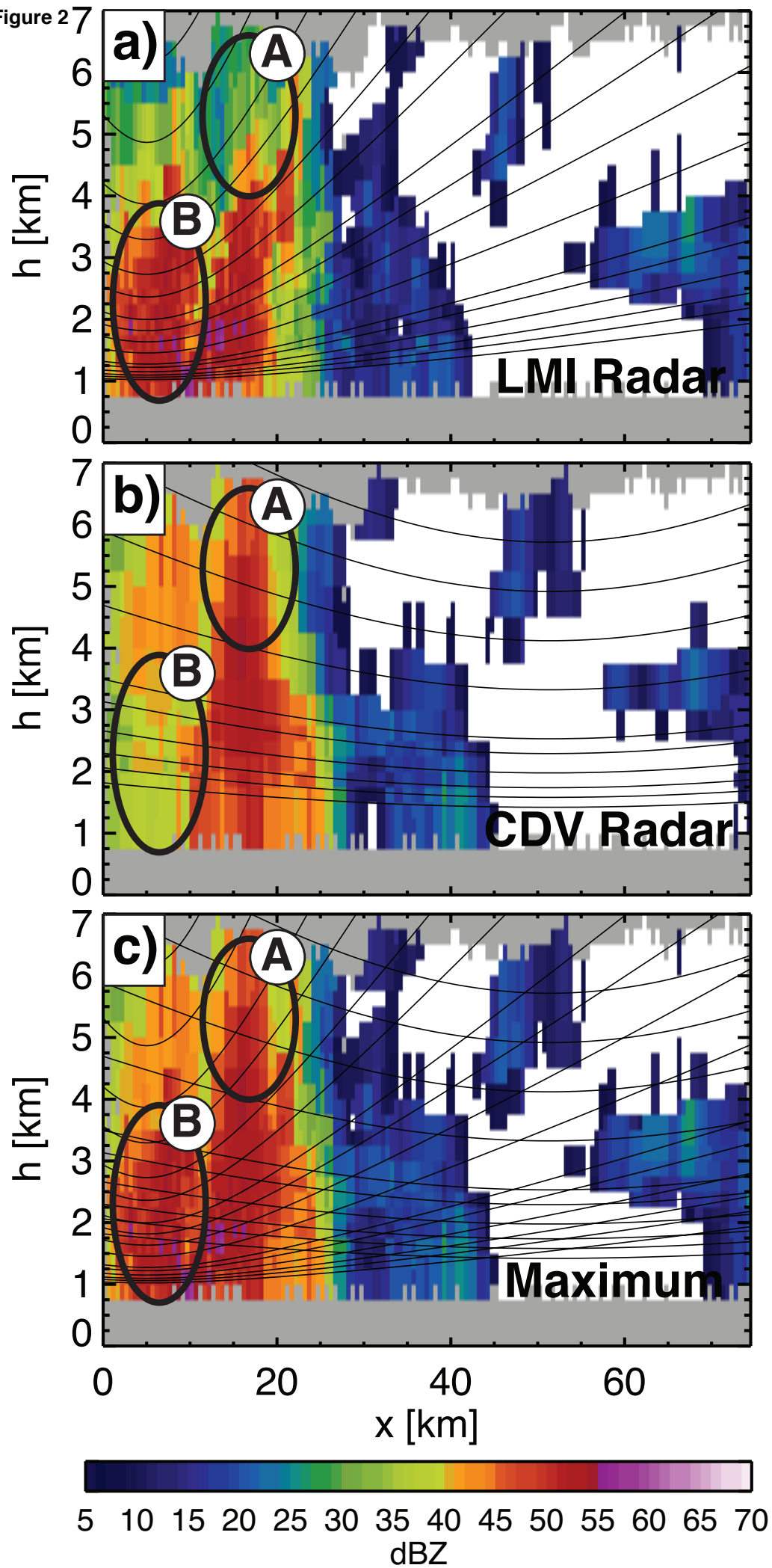
Figure 2

Figure 3

Figure 4

Figure 5

Elevation: 0.6°

Figure 6

Elevation: 0.6°

Figure 7

Elevation: 0.6°

Elevation: 0.6°

Reflectivity [dBZ]

Elevation: 0.6°

Elevation: 0.6°

PIA [dB]

Figure 8

Height: 1.50 km

Height: 2.00 km

a)

b)

x = 20.00 km

c)

y = 50.00 km

d)
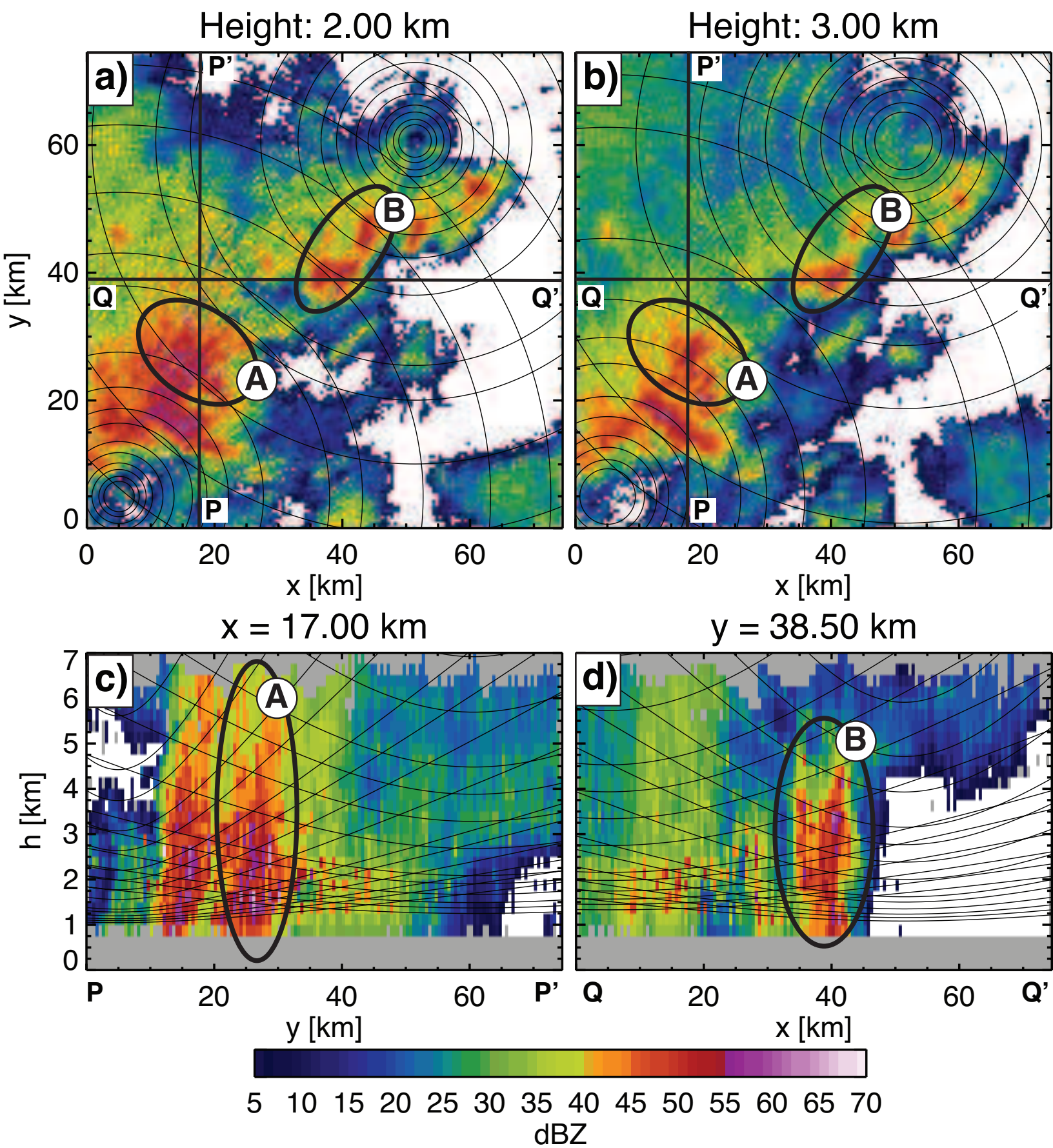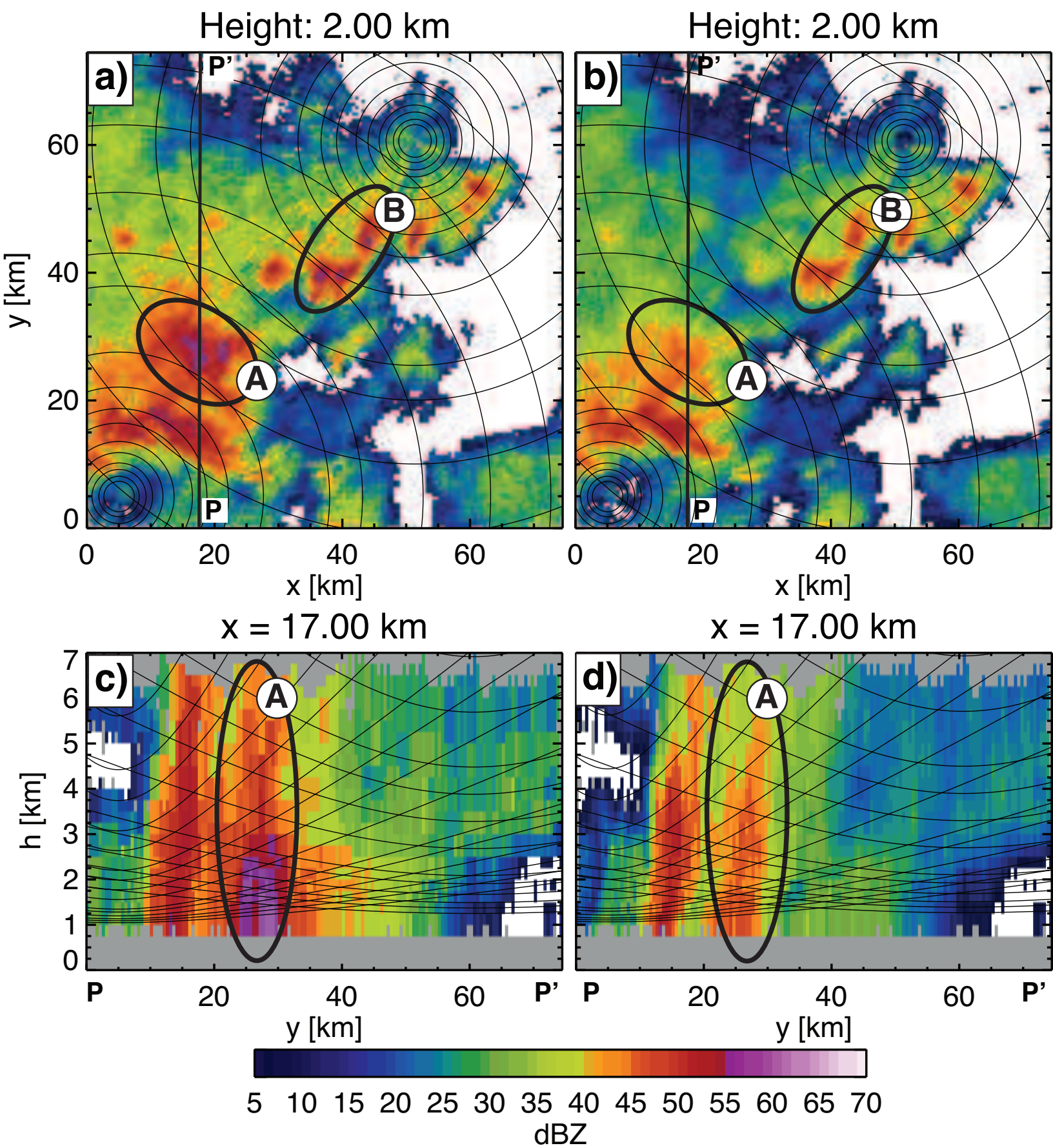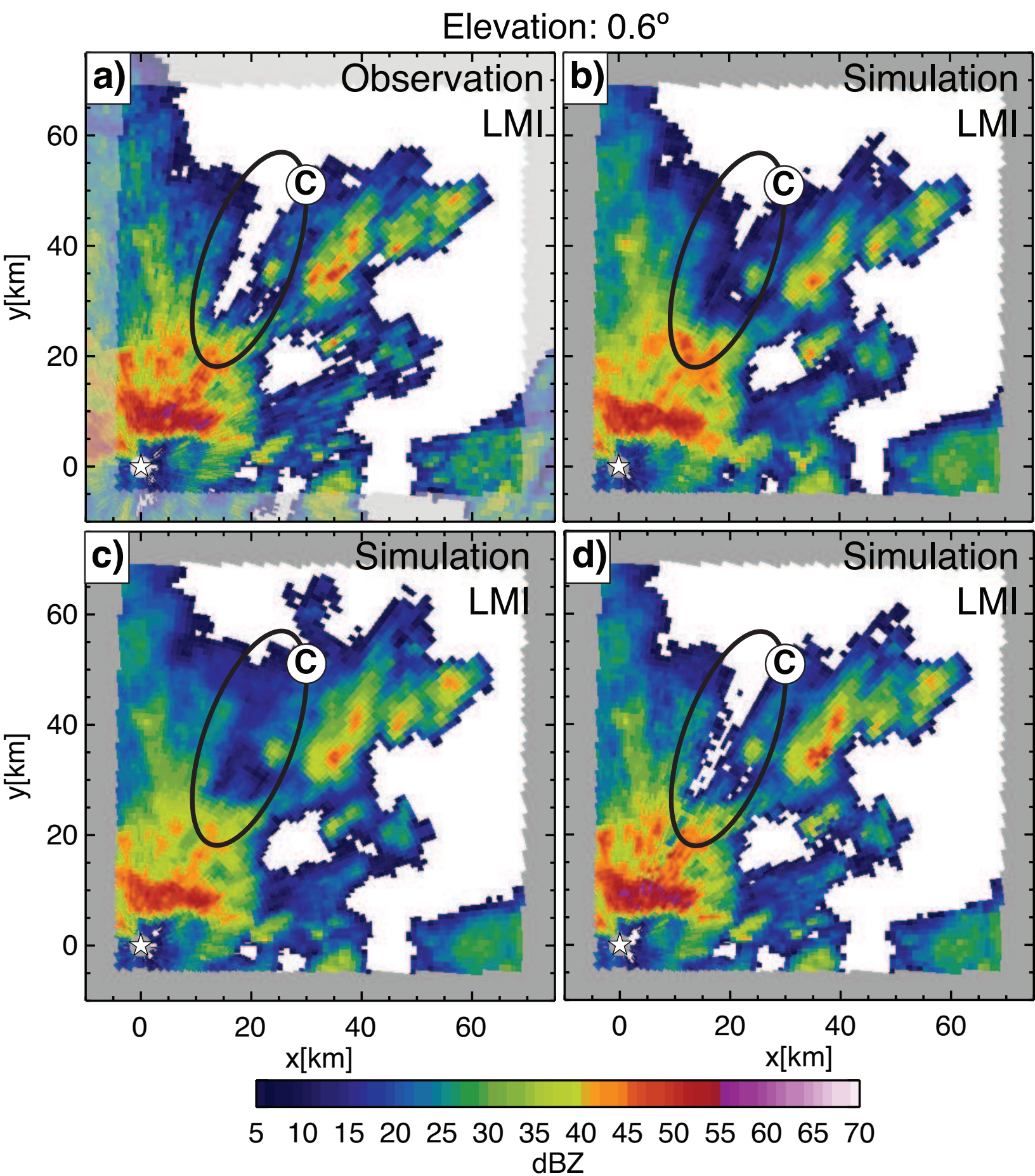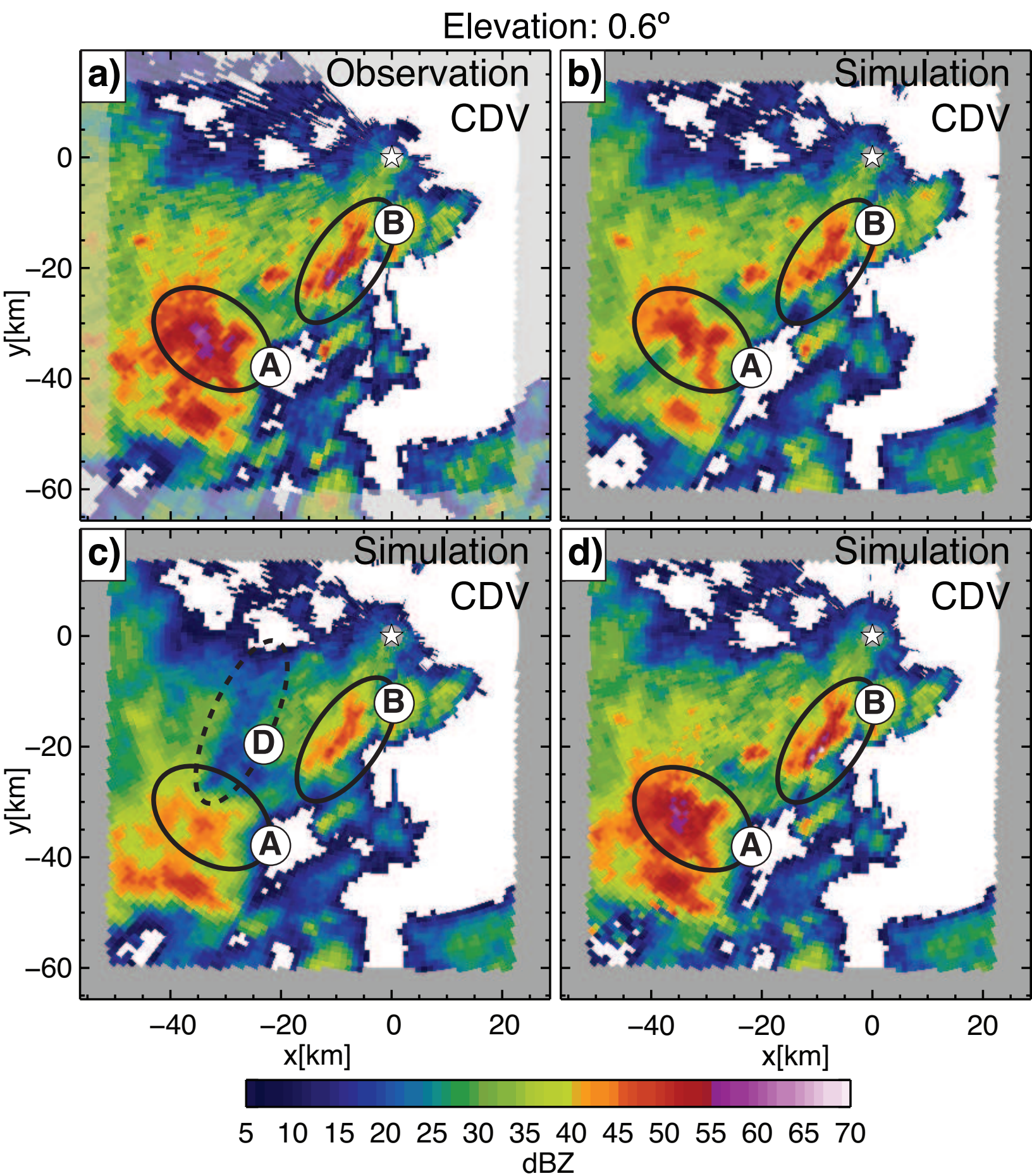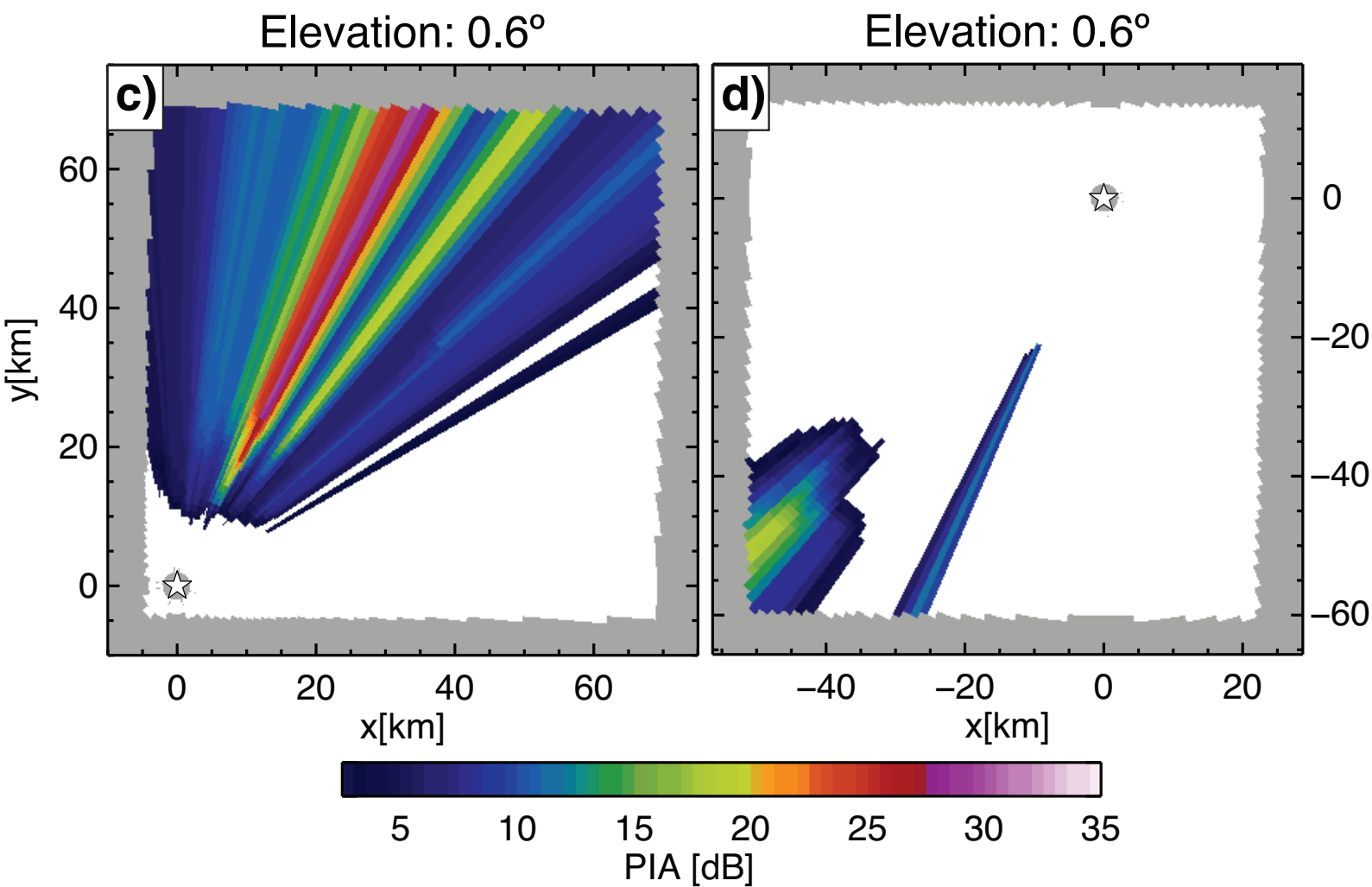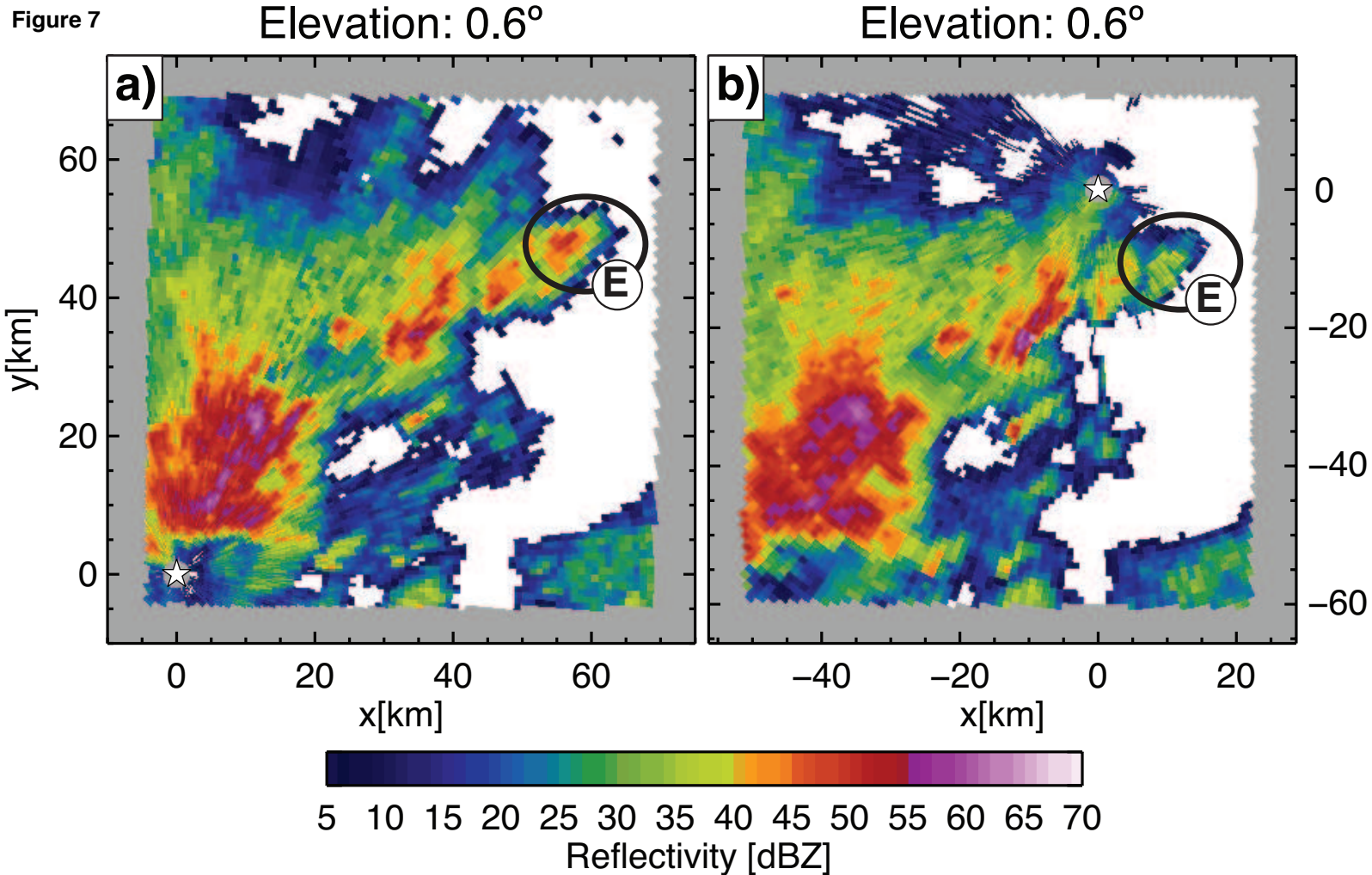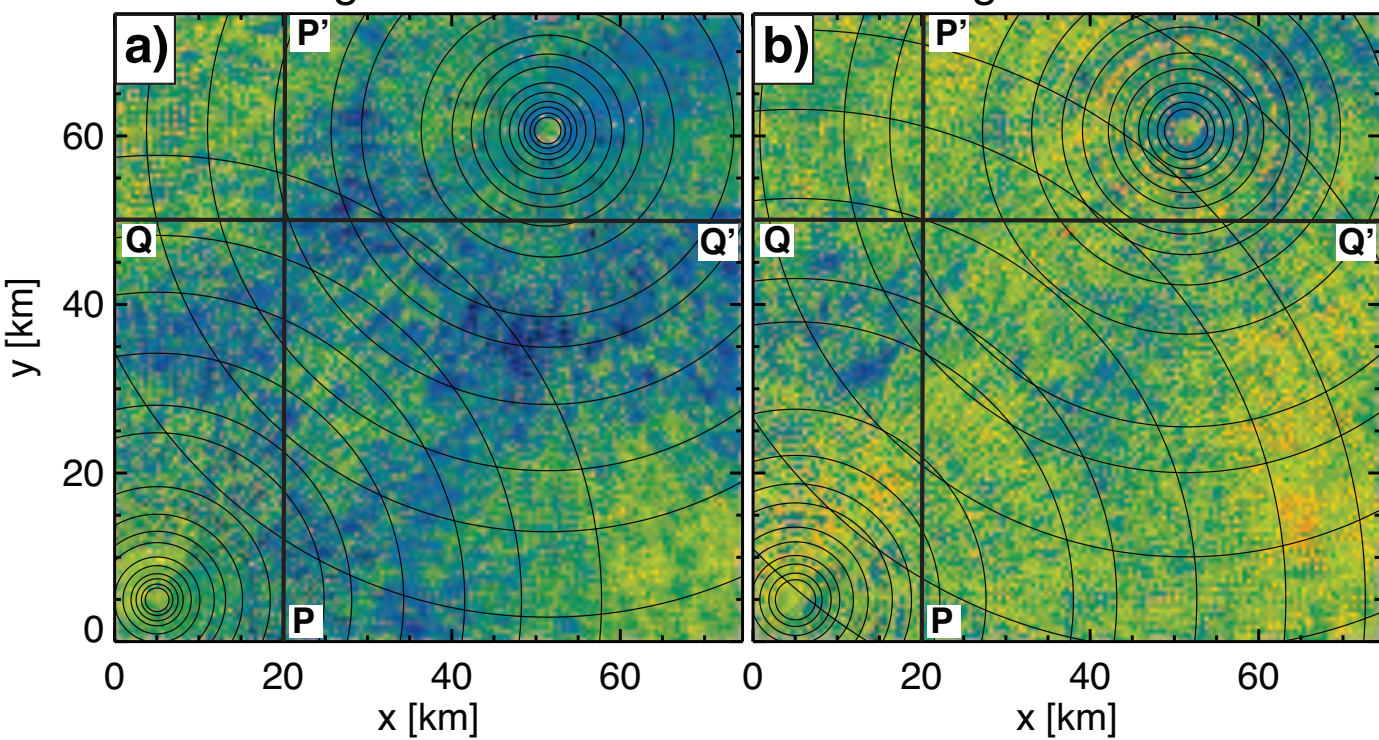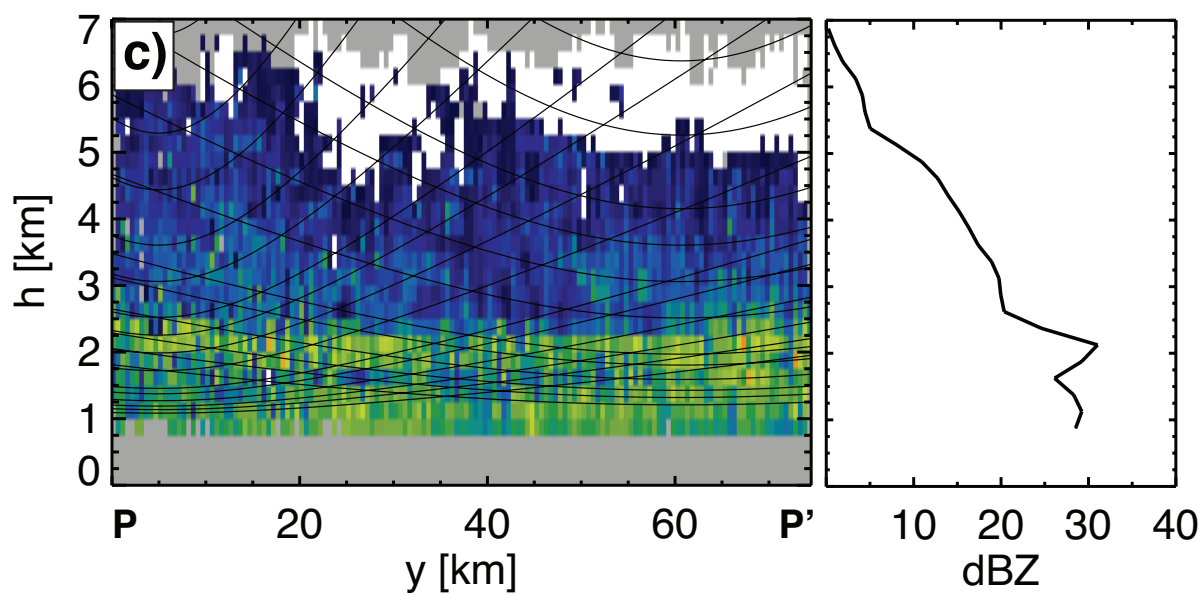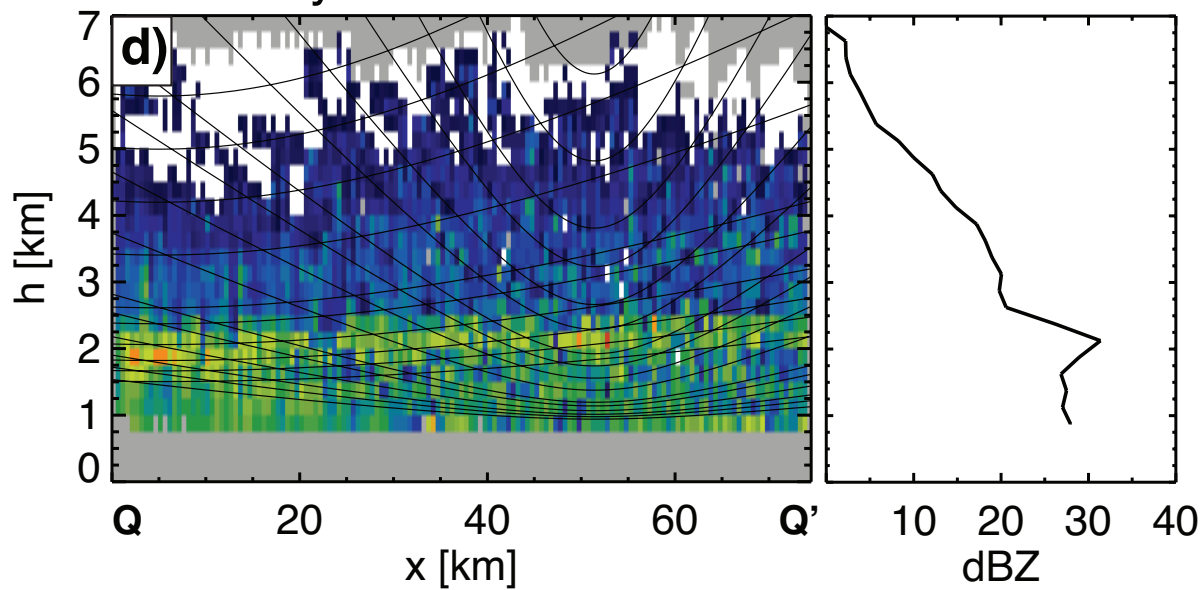
Figure 9

Figure 10

Figure 11

a)

BAR Radar
02/11/2008 0330 UTC
Elevation: 0.5°

Observation

b) Simulation (M2)
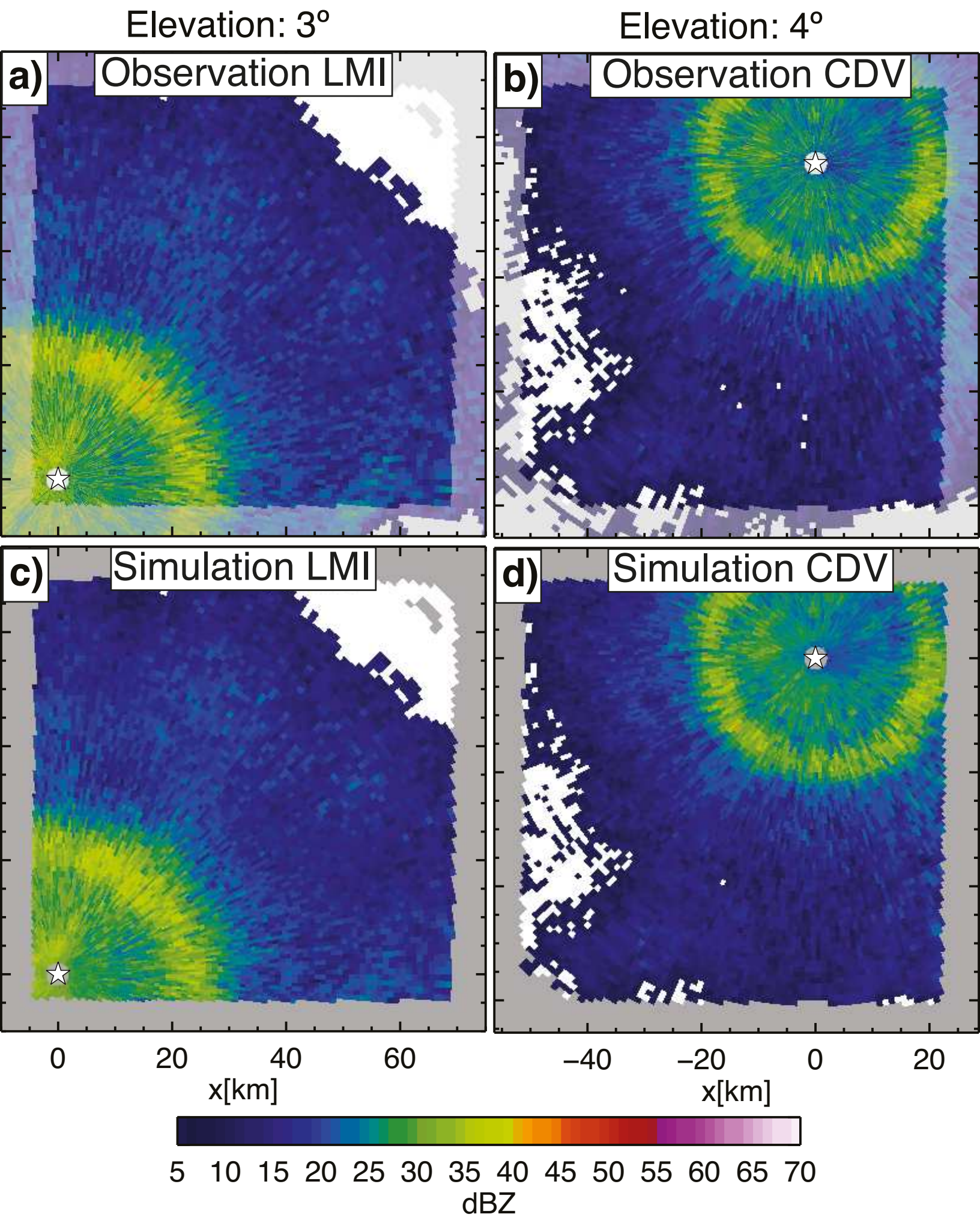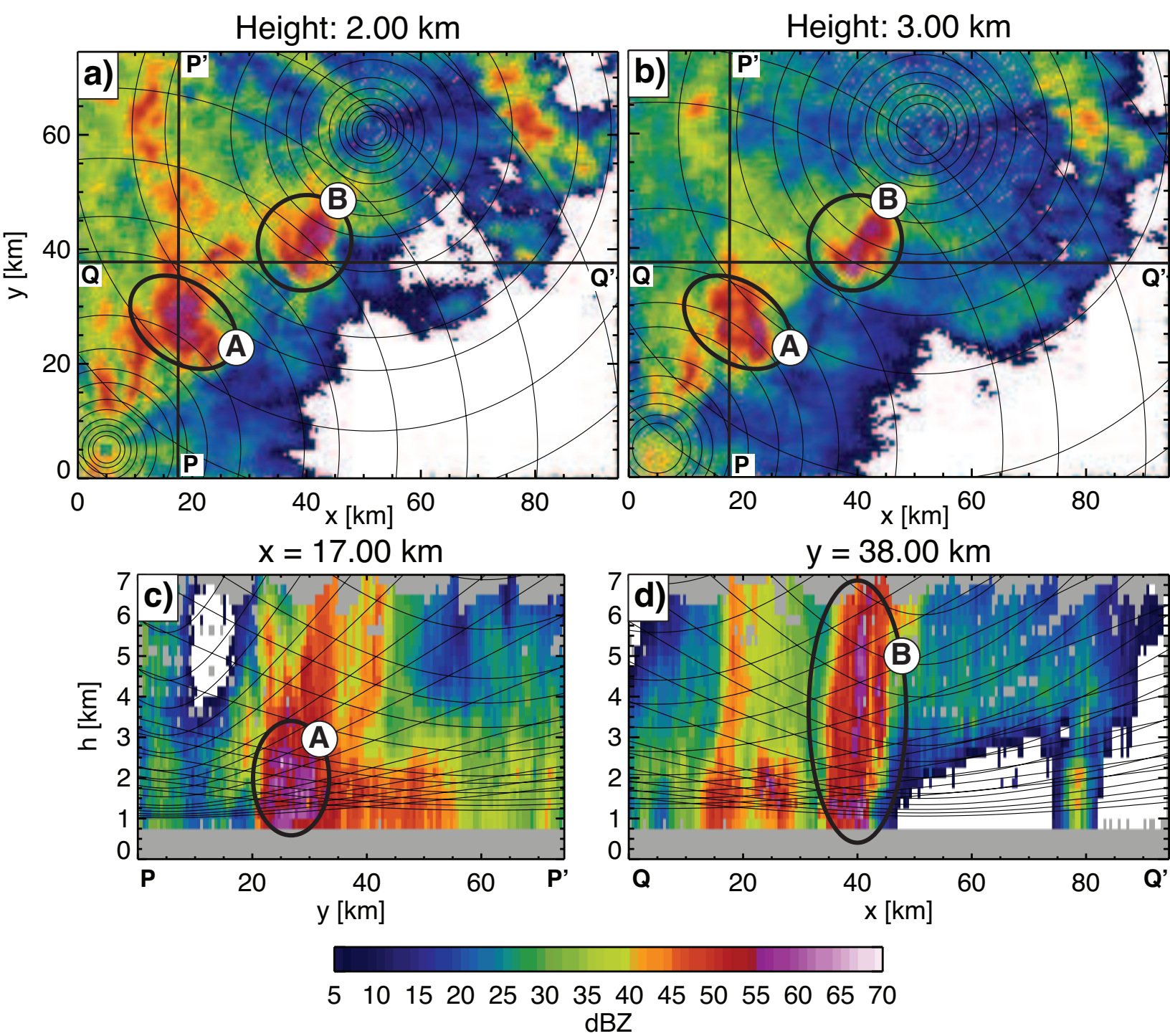
c) Simulation (Inverse method)
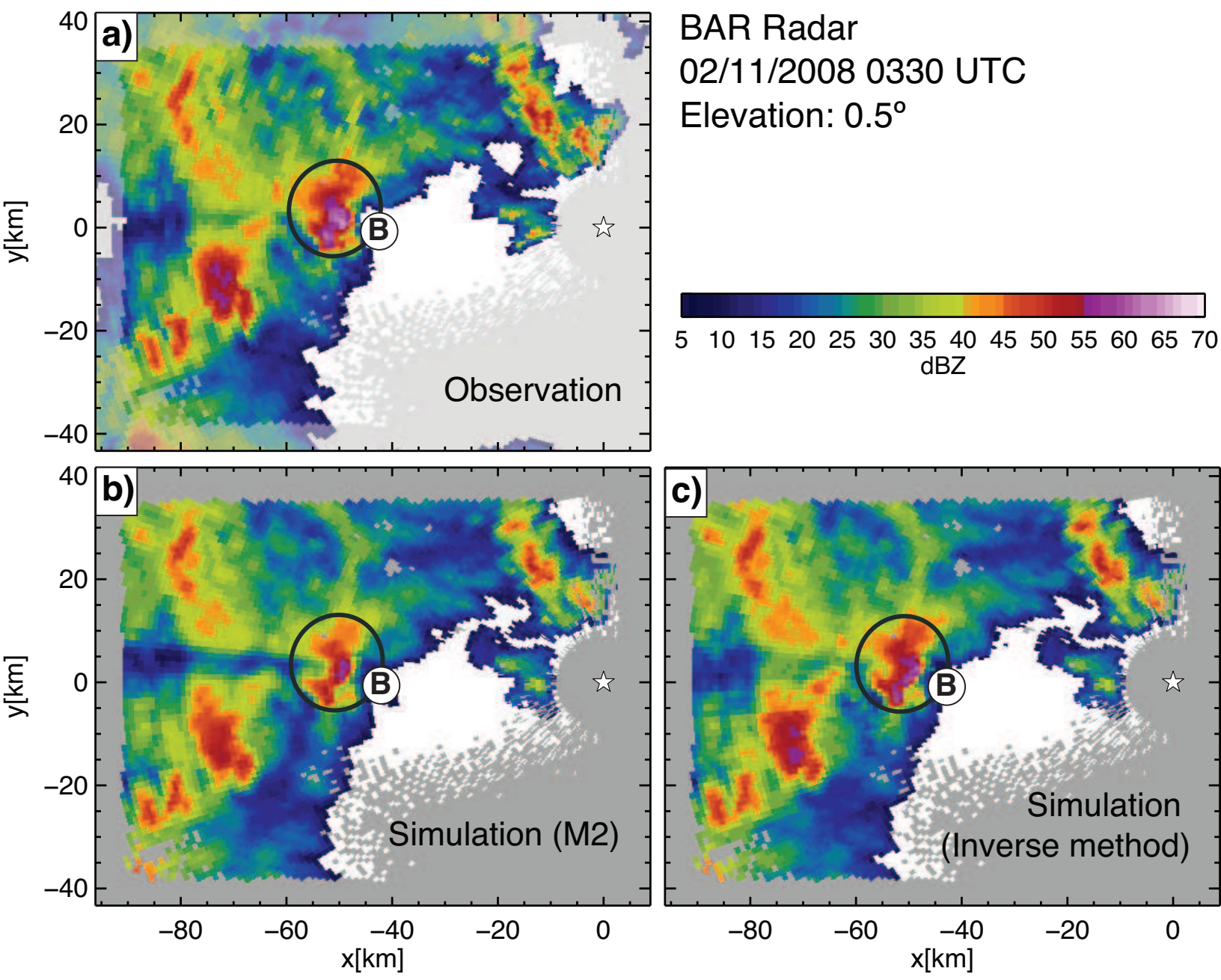
Figure 12

Comparison between observations and simulations over the composites obtained with the techniques: ▬▬ M2 ▬▬ Inverse method
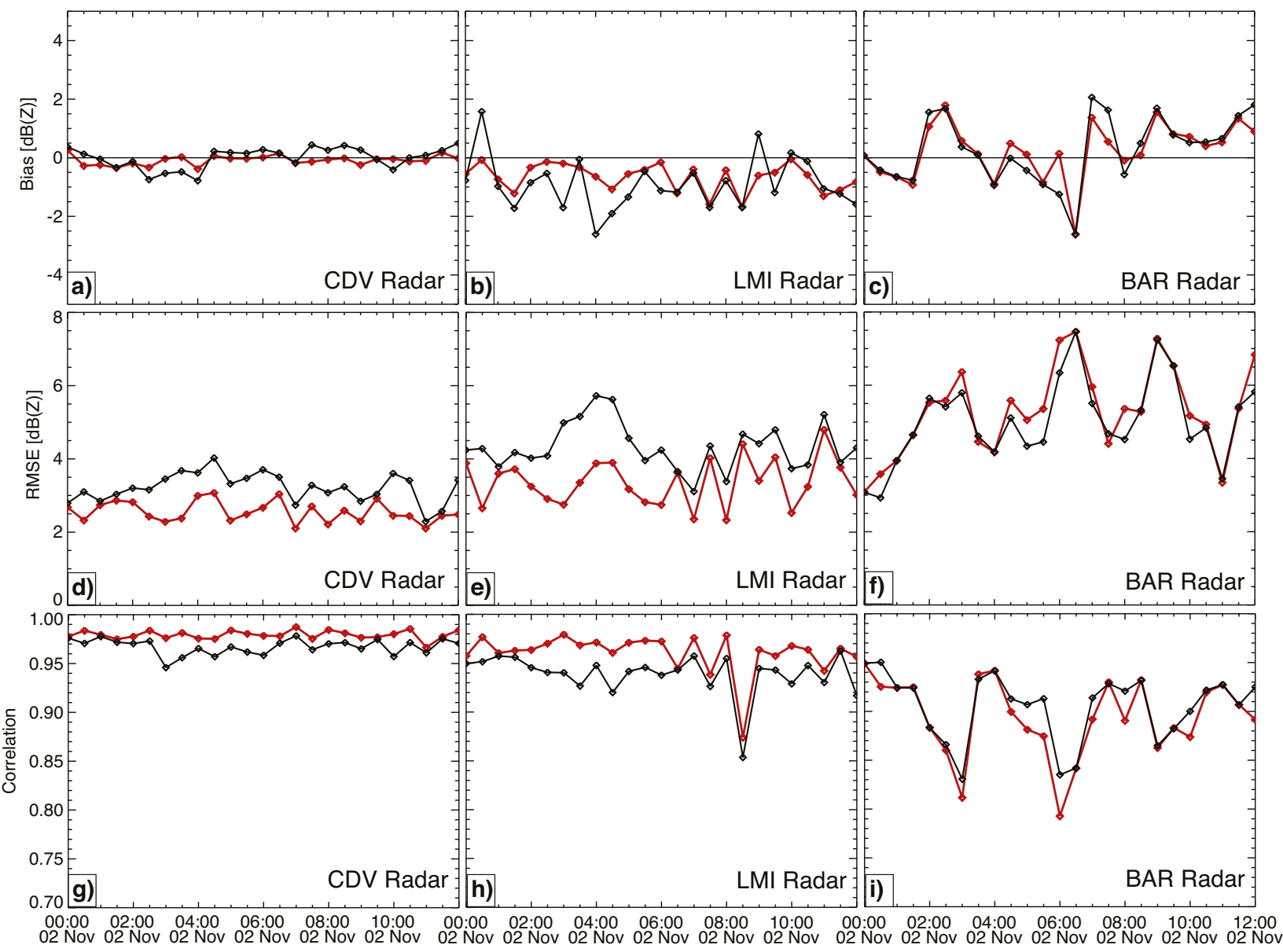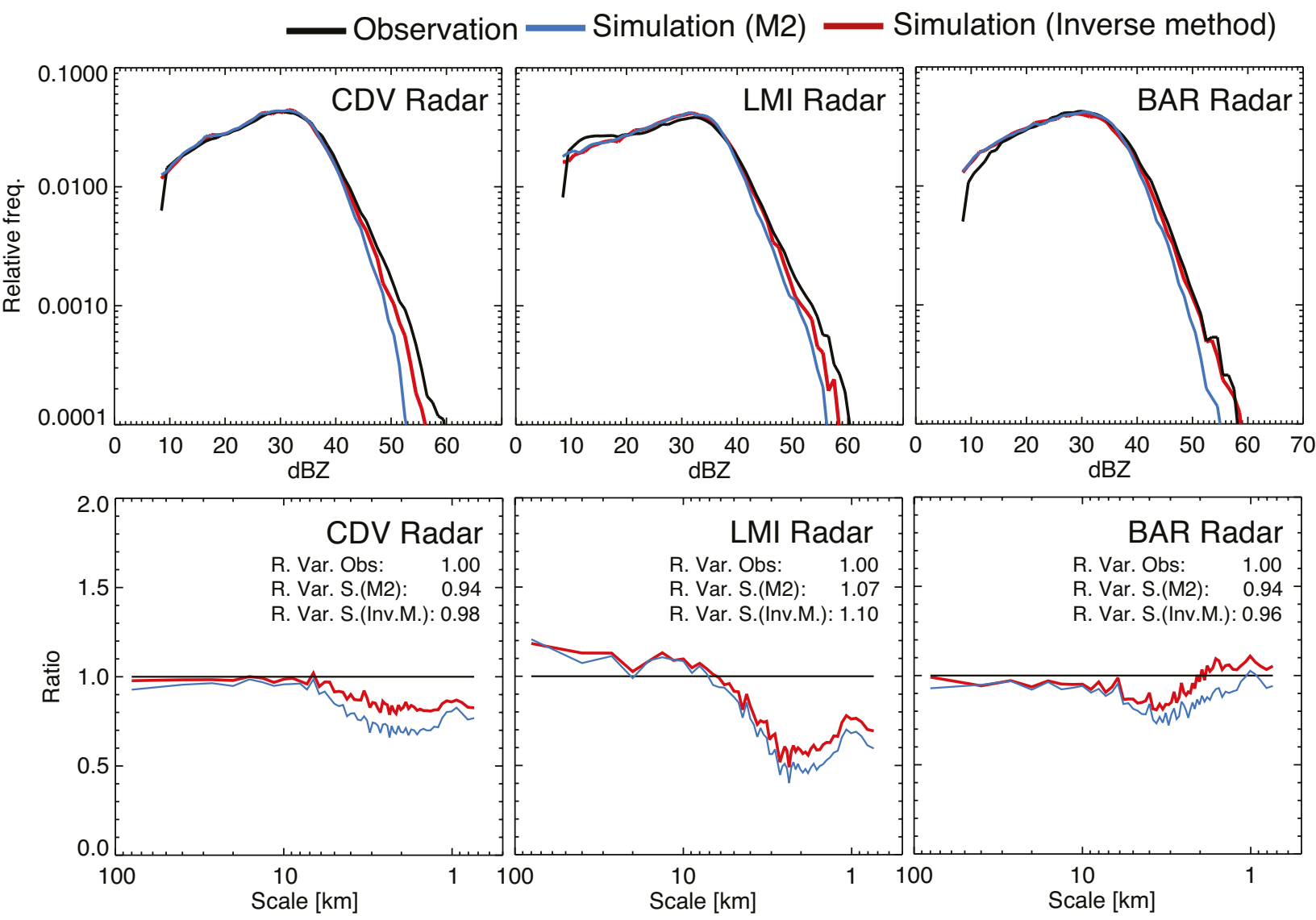
Figure 13

Figure 14

Figure 15